Monthly Notices
of the
ROYAL ASTRONOMICAL SOCIETY

MNRAS **495,** 4924–4942 (2020)
Advance Access publication 2020 June 2

doi:10.1093/mnras/staa1465

A PSF-based Approach to TESS High quality data Of Stellar clusters (PATHOS) – II. Search for exoplanets in open clusters of the Southern ecliptic hemisphere and their frequency

D. Nardiello [1,2★] G. Piotto,[2,3] M. Deleuil,[1] L. Malavolta [3] M. Montalto,[2,3] L. R. Bedin [2] L. Borsato [2] V. Granata,[2,3] M. Libralato [4] and E. E. Manthopoulou[2,3]

[1]*Aix-Marseille Université, CNRS, CNES, LAM, F-13013 Marseille, France*
[2]*Istituto Nazionale di Astrofisica – Osservatorio Astronomico di Padova, Vicolo dell'Osservatorio 5, I-35122 Padova, Italy*
[3]*Dipartimento di Fisica e Astronomia 'Galileo Galilei', Università di Padova, Vicolo dell'Osservatorio 3, I-35122 Padova, Italy*
[4]*Space Telescope Science Institute, 3800 San Martin Drive, Baltimore, MD 21218, USA*

Accepted 2020 May 20. Received 2020 May 20; in original form 2020 April 22

ABSTRACT

The scope of the project 'A PSF-based Approach to TESS High Quality data Of Stellar clusters' (PATHOS) is the extraction and analysis of high-precision light curves of stars in stellar clusters and young associations for the identification of candidate exoplanets and variable stars. The cutting-edge tools used in this project allow us to measure the real flux of stars in dense fields, minimizing the effects due to contamination by neighbour sources. We extracted about 200 000 light curves of stars in 645 open clusters located in the Southern ecliptic hemisphere and observed by *TESS* during the first year of its mission. We searched for transiting signals and we found 33 objects of interest, 11 of which are strong candidate exoplanets. Because of the limited SNR, we did not find any Earth or super-Earth. We identified two Neptune-size planets orbiting stars with $R_\star < 1.5\,R_\odot$, implying a frequency $f_\star = 1.34 \pm 0.95$ per cent, consistent with the frequency around field stars. The seven Jupiter candidates around stars with $R_\star < 1.5\,R_\odot$ imply a frequency $f_\star = 0.19 \pm 0.07$ per cent, which is smaller than in the field. A more complete estimate of the survey completeness and false positive rate is needed to confirm these results. Light curves used in this work will be made available to the astronomical community on the Mikulski Archive for Space Telescope under the project PATHOS.

Key words: techniques: image processing – techniques: photometric – planetary systems – open clusters and associations: general.

1 INTRODUCTION

In our Galaxy, there are more than 1500 globular clusters, open clusters, and stellar associations. These objects can comprise up to several hundreds thousand stars covering all ranges of spectral classes and stellar evolutionary stages and have ages that span from few million years to almost the age of the Universe. Their chemical properties reflect the chemical evolution of the Milky Way. For these stars, we can extract with high accuracy essential pieces of information, like the radius, the mass, the chemical content, and the age, i.e. parameters that suffer usually of large uncertainties for many field stars. The possibility of measuring stellar host parameters with high precision makes the search for exoplanets around cluster stars, and their frequency, of particular interest, especially if we want to comprehend how they formed and evolved in different environments.

Despite the large number of stars in stellar clusters and associations, only a small fraction of known (candidate) exoplanets orbit these stars. These objects have been found by looking for transits in the light curves of the cluster/association members and/or analysing their radial velocities. To date, 28 exoplanets with status between candidate and confirmed have been discovered in stellar clusters and associations. The first exoplanet discovered in a stellar cluster, the Hyades, was found by Sato et al. (2007); since then, other three exoplanets and an exoplanetary system have been found in this open cluster, by using both radial velocities (Quinn et al. 2014) and *Kepler*/*K2* (Howell et al. 2014) light curves (David et al. 2016a; Mann et al. 2016a, 2018; Ciardi et al. 2018; Vanderburg et al. 2018) The first two transiting exoplanets in an open cluster, NGC 6811, were discovered by Meibom et al. (2013) using *Kepler* main mission data (Borucki et al. 2010). The Praesepe cluster hosts eight candidate/confirmed exoplanets and an exoplanetary system (Quinn et al. 2012; Barros, Demangeon & Deleuil 2016; Libralato et al. 2016b; Malavolta et al. 2016; Obermeier et al. 2016; Pope, Parviainen & Aigrain 2016; Mann et al. 2017; Pepper et al. 2017;

★ E-mail: domenico.nardiello@lam.fr

Gaidos et al. 2020). A transiting exoplanet has been discovered by Curtis et al. (2018) in the 3-Gyr-old open cluster Ruprecht 147. No transiting exoplanets around members of the old open cluster M 67 have been reported by Nardiello et al. (2016a), despite the fact that Brucalassi et al. (2014, 2016, 2017) found an excess of hot Jupiters by using radial velocity measurements. Noteworthy, the unusual null detection of exoplanets around Pleiades members has been reported by Gaidos et al. (2017) and Mann et al. (2017). Some exoplanets have also been found in young associations and moving groups. The first one is K2-33b, orbiting a pre-main-sequence star that belongs to the Upper Scorpius OB association (David et al. 2016b; Mann et al. 2016b). Exoplanets were also found in the associations Cas-Tau (EPIC 247267267 b; David et al. 2018) and Tuc-Hor (DS Tuc A b; Benatti et al. 2019; Newton et al. 2019).

Among the previously mentioned exoplanets in stellar clusters and associations, 18 are transiting exoplanets and, excluding DS Tuc A b, they were all discovered by using data collected with *Kepler*. But only a handful of clusters and associations were observed during the *Kepler* main and *K2* missions, and the number of studied cluster members is limited to few thousand stars. The opportunity that the *Transiting Exoplanet Survey Satellite* (*TESS*; Ricker et al. 2015) is giving us is without equal: At the end of its 2-yr nominal mission, this satellite will have observed more than 80 per cent of the sky, thus including almost all the known clusters and associations.

In *TESS* observations, the large part of the cluster members fall in 30-min cadence-stacked frames, called full frame images (FFIs), collected during 27-d campaigns; each campaign covers a sector of the sky of $24 \times 96\,\mathrm{deg}^2$. One of the major problems to be addressed in the extraction of high-precision light curves of cluster members from *TESS* FFIs is related to their low angular resolution ($\sim$21 arcsec pixel^{-1}). In fact, even low-density stellar clusters appear crowded in *TESS* images, where their members are likely blended among each other or with field stars. In these conditions, the extraction of light curves using simple aperture photometry is not reliable because contamination and blending effects prevail.

In the last years, many approaches have been developed for the extraction of high-precision light curves of stars in crowded regions, based on the use of the point spread functions (PSFs; Nardiello et al. 2015a; Libralato et al. 2016a) or the difference imaging analysis (Alard & Lupton 1998; Chang, Byun & Hartman 2015; Soares-Furtado et al. 2017; Bouma et al. 2019; Wallace et al. 2019; Soares-Furtado et al. 2020). In the first paper of this series, we presented our project 'A PSF-based Approach to TESS High Quality data Of Stellar clusters' (PATHOS; Nardiello et al. 2019, hereafter Paper I), aimed at the extraction of high-precision light curves for stars in stellar clusters (open and globular clusters) and young associations. Our approach of light-curve extraction, already widely tested on ground-based *Kepler* and also *TESS* data, is based on the use of empirical PSFs and an input catalogue to measure the flux of a given star after having suppressed the contribution of its neighbours. In this way, we are able to measure the real flux of the target star, minimize the dilution effects due to the contamination by neighbour sources (essential in the search for exoplanetary transits), and extract high-precision photometry even for stars close to the *TESS* limiting magnitude ($T \sim 17$).

In Paper I, we successfully applied our method to an extreme case of crowded region, a field containing the globular cluster 47 Tuc, which includes Galactic and Small Magellanic Cloud stars. We searched for exoplanets and variable stars among all the extracted light curves, finding one candidate exoplanet (a hot Jupiter around a field star, PATHOS-1) and many new variable stars along the red and asymptotic giant branch sequences of 47 Tuc. For this work, we applied our PSF-based approach to extract high-precision light curves for stars belonging to open clusters in the Southern ecliptic hemisphere and listed in the catalogue published by Cantat-Gaudin et al. (2018, Section 2). We analysed these light curves searching for transit signals, and we selected the most promising transiting objects and validated them with a series of vetting tests (Section 3). We modelled the transits of the candidate exoplanets to derive their parameters (Section 4), and analysed their dependence on cluster properties (Sections 4 and 5). We also estimated the observed and expected occurrence rate of exoplanets and discussed our results in Section 6.

2 OBSERVATIONS AND DATA REDUCTION

This work is focused on the open clusters located in the Southern ecliptic hemisphere and that were observed by *TESS* in Sectors 1–13. In this work we used observations carried out by *TESS* in a period of $\sim$1 yr (357 d), between 2018 July 25 and 2019 July 17; the total number of FFIs used for the extraction of the light curves is 245 576, which are all the downloadable FFIs for the Sectors 1–13.[1]

The light-curve extraction has been performed using an improved version of IMG2LC, the software described in Paper I. The three main ingredients of our approach are (i) FFIs, (ii) PSFs, and (iii) input catalogue. In the following, we give a short description of the input catalogue adopted and our pipeline.

2.1 The input catalogue

Our pipeline extracts the light curves of all the sources whose coordinates are listed in an input catalogue. For this work, we used as input the catalogue published by Cantat-Gaudin et al. (2018). This catalogue contains, for 1229 clusters, a list of stellar cluster members, whose membership probabilities are calculated by using *Gaia* DR2 proper motions and parallaxes (Gaia Collaboration et al. 2018). From this catalogue, we selected a sub-sample of stars having magnitude $G < 17.5$ and (a conservative) ecliptic latitude $\beta < -4°$, which corresponds to the fields covered by *TESS* in the Sectors 1–13. In this way, we selected a total of 189 090 cluster members, although $\sim$13.9 per cent of them are not observed by *TESS* because they fall between CCD/Camera gaps or between sector gaps, or because they are outside the field of view of *TESS* observations, as shown in Fig. 1. On the other hand, $\sim$1/4 of the stars in the input catalogue are observed in more than one sector. Finally, we extracted a total of 219 256 light curves of stars in 645 open clusters. In the following analysis, we excluded the members of NGC 1901, an open cluster in the *TESS* continuous viewing zone; this cluster is the only one observed in all the 13 Sectors, and will be the subject of a future work (Manthopoulou et al., in preparation).

2.2 Light-curve extraction

For the extraction of the light curves from *TESS* FFIs, we adopted the PSF-based approach developed by Nardiello et al. (2015a, 2016b) for the ground-based data collected with the Asiago Schmidt Telescope 67/92 cm. This pipeline was also adapted to *Kepler*/*K2* space-based data set by Libralato et al. (2016a, see also Libralato

[1] https://archive.stsci.edu/tess/bulk_downloads-/bulk_downloads_ffi-tp-lc-dv.html.

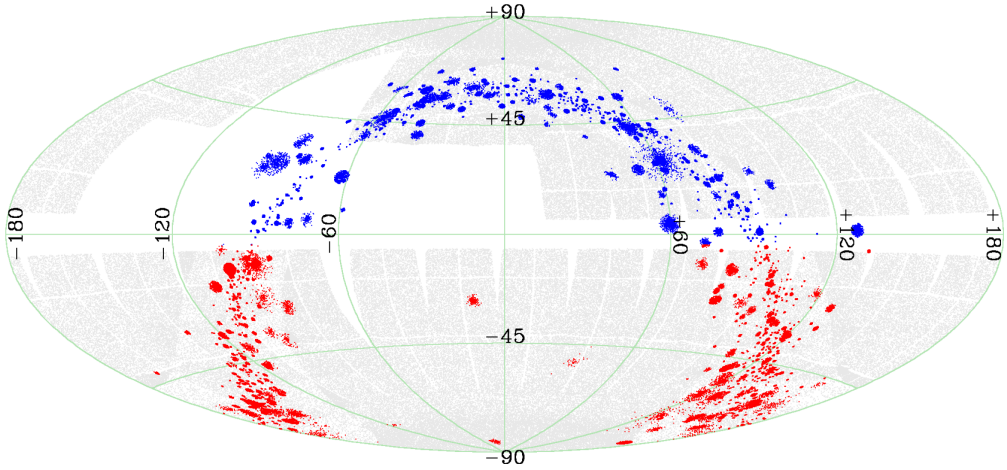

Figure 1. Aitoff projection in ecliptic coordinates of the *TESS* observations: Grey points represent the sources observed in 2-min cadence mode in Sectors 1–24; red/blue points show the open cluster members for which we propose to extract the light curves in our project; and red points show the stars in the input catalogue used in this work.

et al. 2016b; Nardiello et al. 2016a) and finally to *TESS* data in Paper I.

As a first step, the routine transforms the positions and the luminosities of the stars in the input catalogue into the reference system of a single image. For all the stars in the input catalogue, it transforms the (α, δ)-coordinates into the image reference system using the transformation coefficients listed in the FITS header of the single FFI.

In a second step, the software calculates the photometric zero-point between the calibrated and instrumental *TESS* magnitudes as follows: For the 200 brightest, not saturated stars of each FFI, it extracts the PSF-fitting magnitudes, $T_{\rm inst}$, and calculates the 3.5σ-clipped mean value of $T^i_{\rm cal} - T^i_{\rm inst}$, with $i = 1, ..., 200$ and $T_{\rm cal}$ the calibrated *TESS* magnitudes calculated by using *Gaia* DR2 magnitudes and the equation in Stassun et al. (2019).

Finally, for each star in the input catalogue, the routine searches in the *Gaia* DR2 catalogue (Gaia Collaboration 2018) all the neighbours located between 0.5 and 20 *TESS* pixels from the target star and having $T < 17.5$, and transforms their positions and luminosities into the FFI reference system, as described above. The software models the neighbour sources by using the local PSF and the transformed positions and luminosities, and it subtracts these models from the original FFI, as shown in Fig. 2. After the neighbour subtraction, our software performs PSF fitting and four different aperture photometries (1-, 2-, 3-, and 4-pixel radius) of the target star.

2.3 Systematic effects correction

Variations in the spacecraft, detector, and environment conditions affect the quality of the light curves, introducing systematic artefacts. These systematic trends are common to all the stars of a given *TESS* Camera/CCD/Sector, and can be corrected using orthonormal functions called cotrending basis vectors (CBVs).

To extract the CBVs, we combined two samples of light curves: (i) the light curves of the stars in the input catalogue described in Section 2.1 and (ii) the light curves of the stars also observed in 2-min cadence mode (grey points of Fig. 1) and extracted from FFIs with our pipeline. We extracted the second sample of light curves to increase the number of bright stars in our list and extract better CBVs associated with 3- and 4-pixel aperture photometries.

To extract the CBVs, we followed a procedure similar to that described in Paper I: For each star and for each photometric method, we calculated the raw rms.[2] On the basis of the rms distributions, we identified the magnitude interval where each photometric method works better and we selected the best measured stars on the basis of their rms values as follows: For each photometric method, we divided the rms distributions in bins of width 0.75 T magnitude and we estimated in each magnitude interval the 3.5σ-clipped mean value of the rms. We interpolated the binned points with a spline: For each photometric method, we selected the magnitude interval where the mean rms distribution is lower compared to the other distributions. For the stars that passed the first selection criteria, we calculated the median of the correlation coefficients between a given light curve and the light curves of the other stars. We kept all the stars with a median correlation coefficient >50 per cent, and we iterated other two times, restarting from the calculation of the median correlation coefficient, and considering at each iteration only the stars that passed the selection criteria of the previous iteration. With the surviving stars, we extracted 20 CBVs for each photometric method using the single value decomposition. On average, CBVs are obtained by using between 200 and 300 stars.

To correct the light curves, we used the Levenberg–Marquardt method (Moré, Garbow & Hillstrom 1980) to find the coefficients A_i that minimized the expression

$$F^j_{\rm raw} - \sum_i \left(A_i {\rm CBV}^j_i\right), \quad (1)$$

with $F^j_{\rm raw}$ the raw flux of the light curve at the epoch j, and ${\rm CBV}_i$ the ith CBV, with $i = 1, ..., 20$. We changed the number of CBVs applied to obtain the correction from 1 to 20, and for each light curve and photometric method, we selected the number of CBVs whose correction gives the lower Akaike's information criterion (AIC) score.

Bottom panels of Fig. 2 show the light curves of *Gaia* DR2 3111381928222301184 before (black points) and after (red points) correction, in the case of PSF-fitting photometry and 3-

[2]Defined as the 68.27th percentile of the sorted residual from the median value of the light curve.

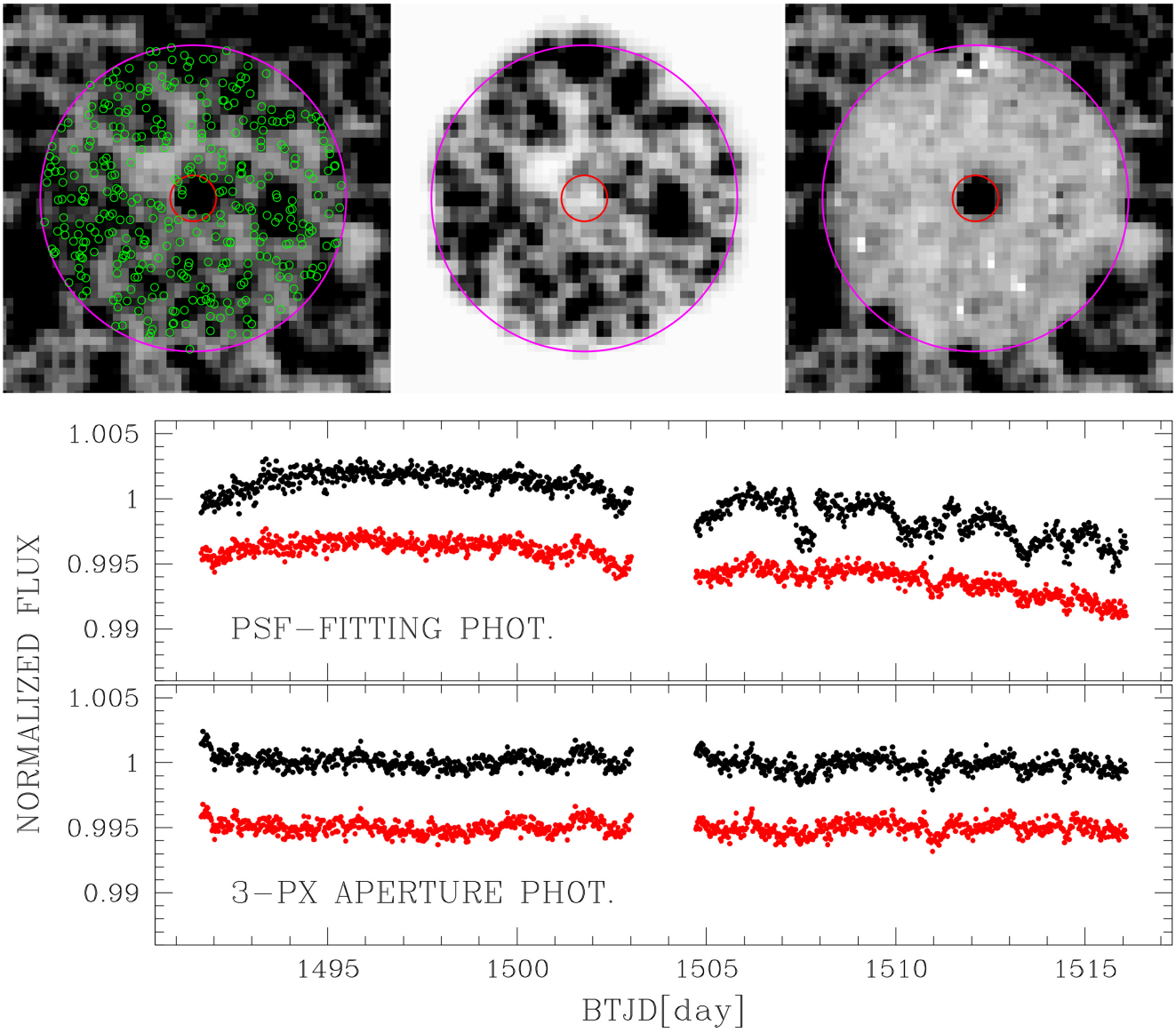

Figure 2. From FFI to the final light curve. Top panels: example of neighbour subtraction. The left-hand panel shows the original FFI (`tess2019009222936-s0007-1-1-0131-s_ffic.fits`) centred on the star *Gaia* DR2 3111381928222301184, a possible cluster member of Gulliver 47; red circles show the photometric aperture used to analyse this star, and green circles show the neighbours located within a radius of 20 pixels (magenta circle) from the target star. The middle panel shows the models of the neighbours subtracted from the FFI; the right-hand panel shows the FFI after neighbour subtraction. Bottom panels: the PSF fitting and 3-pixel aperture photometry light curves of the star *Gaia* DR2 3111381928222301184 before (black points) and after (red points) the systematic correction.

pixel aperture photometry: The improvement of the light curve in the case of PSF-fitting photometry is clear, and the rms of the light curve passes from 2.1 to 1.6 mmag.

2.4 Saturated stars

Stars with $T \lesssim 5.5$ are saturated on FFIs, and form a bleeding column. As explained in the TESS Instrument Handbook, the CCDs conserve the electrons even when saturation causes their moving along the columns neighbouring the pixel where they were generated. To recover the charge along the bleeding column, we used the technique described in Gilliland (2004) and Gilliland, Rajan & Deustua (2010), and already tested in many works based on *Hubble Space Telescope* data (see, e.g. Anderson et al. 2008; Bellini et al. 2017; Nardiello et al. 2018). Briefly, our routine checks if the central pixel and three of the neighbouring pixels have counts $>80\,000\,e^{-}s^{-1}$; in this case, it checks the presence of a bleeding column and retraces its shape. Finally, it adds the contribution that comes from the bleeding columns to the flux calculated inside an aperture of radius 5.5 pixels centred on the star. In the case of saturated stars, the routine did not perform neighbour subtraction and we did not correct for systematic trends because the sample of saturated (and not variable) stars is too small to extract CBVs. Fig. 3 shows the saturated star *Gaia* DR2 5290818758516639104 ($T \sim 3.1$) on an FFI (left-hand panel) and its light curve extracted from five sectors (right-hand panel). The standard deviation from the mean value of the light curve, after removing the contribution of the variability, is ∼26 ppm.

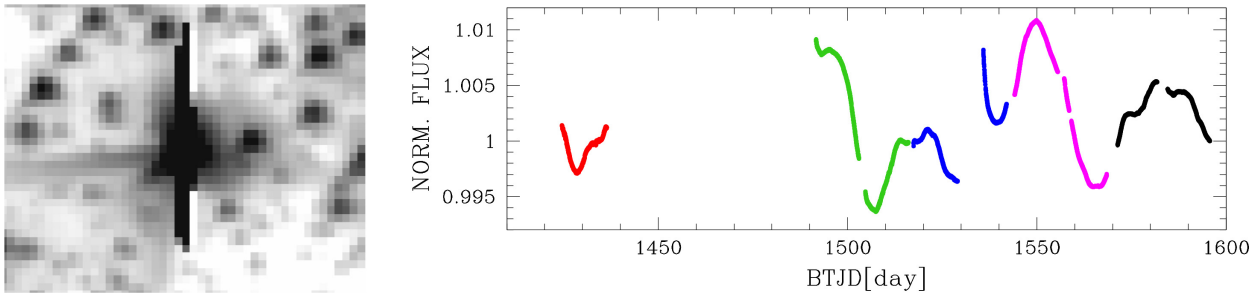

Figure 3. The left-hand panel shows the saturated star *Gaia* DR2 5290818758516639104 on the FFI `tess2019010175936-s0007-4-1-0131-s_ffic.fits`. The right-hand panel shows its light curve extracted from Sectors 4 (red), 7 (green), 8 (blue), 9 (magenta), and 10 (black).

2.5 Data release

All the light curves extracted in this work are released on the Mikulski Archive for Space Telescopes (MAST) as a High Level Science Product (HLSP) under the project PATHOS[3] (DOI: 10.17909/t9-es7m-vw14). Each light curve (in FITS and ASCII format) contains the epoch in TESS Barycentric Julian Day (BTJD), the five extracted raw and corrected photometries (PSF fitting, and 1-, 2-, 3-, and 4-pixel aperture), the value of the local sky, the position (x, y) on the image, and the data quality flag `DQUALITY` (see TESS Science Data Products Description Document for details). All the main information on the star extracted from the *Gaia* DR2 catalogue (Gaia Collaboration et al. 2018) and the observations are reported in the header of each light curve.

2.6 Photometric precision

Fig. 4 shows the two quality parameters adopted also in Paper I and previous works of our group: (i) the rms, calculated using the cotrended light curves and defined as the 68.27th percentile of the sorted residual from the median value, obtained by clipping out the outliers in 10 iterations; and (ii) the `P2P` rms (point-to-point), which is not sensitive to intrinsic stellar variability, and obtained calculating the 68.27th percentile of the distribution of the sorted residual from the median value of $\delta F_j = F_j - F_{j+1}$, with F_j and F_{j+1} the flux of the light curve at the epochs j and $j+1$, respectively.

For each photometric method, we derived, for all the extracted light curves, the mean trends of the rms and `P2P` rms as a function of the T magnitude as follows: We divided each parameter distribution in intervals of 0.75 T magnitude and we calculated in each bin the 3.5σ-clipped average of the parameter. Finally, we interpolated the mean values with a cubic spline. Fig. 4 shows these mean trends both for the rms (top panel) and for the `P2P` rms (bottom panel); in the plot, different colours are associated with different photometric methods: Black, magenta, blue, green, and yellow lines correspond to PSF fitting, 1-, 2-, 3-, and 4-pixel aperture photometries, respectively. Red stars are the saturated stars, measured as described in Section 2.4.

We used the `P2P` rms mean trends to select the best photometric method for each light curve: Given a star of magnitude $T_\star$, we have chosen to analyse the light curve extracted with the photometric method that, in $T_\star$, has the lower mean `P2P` rms. On average, for not saturated stars with $T \lesssim 7.0$, we used the 4-pixel aperture photometry; for stars with $7.0 \lesssim T \lesssim 9.0$ and $9.0 \lesssim T \lesssim 10.5$, the best photometric methods are the 3- and 2-pixel aperture photometries, respectively. PSF-fitting photometry works well for stars having $10.5 \lesssim T \lesssim 13.5$; finally, in the faint regime of magnitudes ($T \gtrsim 13.5$), the 1-pixel aperture photometry gives the best results. Gray dashed line in Fig. 4 is the theoretical limit obtained taking into account all the sources of noise [(shot noise, sky, readout-noise (RON), and dark current (DC)], adopting the average values of RON $\sim 9\,e^-$ pixel^{-1}, DC $\sim 1\,e^-$ s^{-1} pixel^{-1}, sky $\sim 150\,e^-$ s^{-1}, and using in different intervals of magnitudes the aperture radius where the light curve shows the lower scatter, on the basis of the considerations done previously. Theoretical limit distributions are, as expected, lower than the mean observed trends; this is mainly due to a combination of different effects, like stellar variability (that mainly affects the rms distributions), variations of the background in the light curves, contamination by, and blending with, not-subtracted sources, etc.

Before the analysis, we excluded all the light curves for which instrumental magnitude $T_{\rm instr}$ is too different from the expected calibrated magnitude $T_{\rm calib}$, by using the following procedure: For each photometric method (and for each Sector), we analysed the $\delta T = T_{\rm instr} - T_{\rm calib}$ distribution, and we excluded all the light curves whose δT value deviates more than 4σ from the mean value. In this way, we excluded all the light curves of stars strongly contaminated by other sources that were not subtracted during the light-curve extraction (e.g. close bleeding columns, hot pixels, background galaxies, or other sources that were not in the *Gaia* DR2 catalogue). We also excluded all the light curves that have <75 per cent of good points (i.e. `DQUALITY` $= 0$ and `FLUX` $\neq 0$). Finally, we analysed 196 231 light curves associated with 147 702 stars.

3 CANDIDATE EXOPLANETS SELECTION

In order to select candidate transiting exoplanets orbiting stellar cluster members, we performed a series of analyses and tests on the light curves selected as described in the previous sections, to identify and remove the large part of false positive events.

As a first step, we removed the variability of the stars. We flattened the light curves using fifth-order splines defined on $N_{\rm knots}$ knots. We calculated two different grid of knots: (i) a knot every 6.5 h, and (ii) a knot every 13 h. In this way, we were able to better model short- and long-period variable stars, but also to prevent the flattening of the transits whose duration is longer than 6.5 h. In this phase, we also '*cleaned*'' each light curve, excluding (i) points whose quality flag was `DQUALITY` > 0, (ii) all the outliers above 3.5σ the median flux, and (iii) the photometric points associated with local sky background higher than $5\sigma_{\rm sky}$ above median value of the sky. Panels (a) and (b) of Fig. 5 show the procedure of flattening of the

[3] https://archive.stsci.edu/hlsp/pathos.

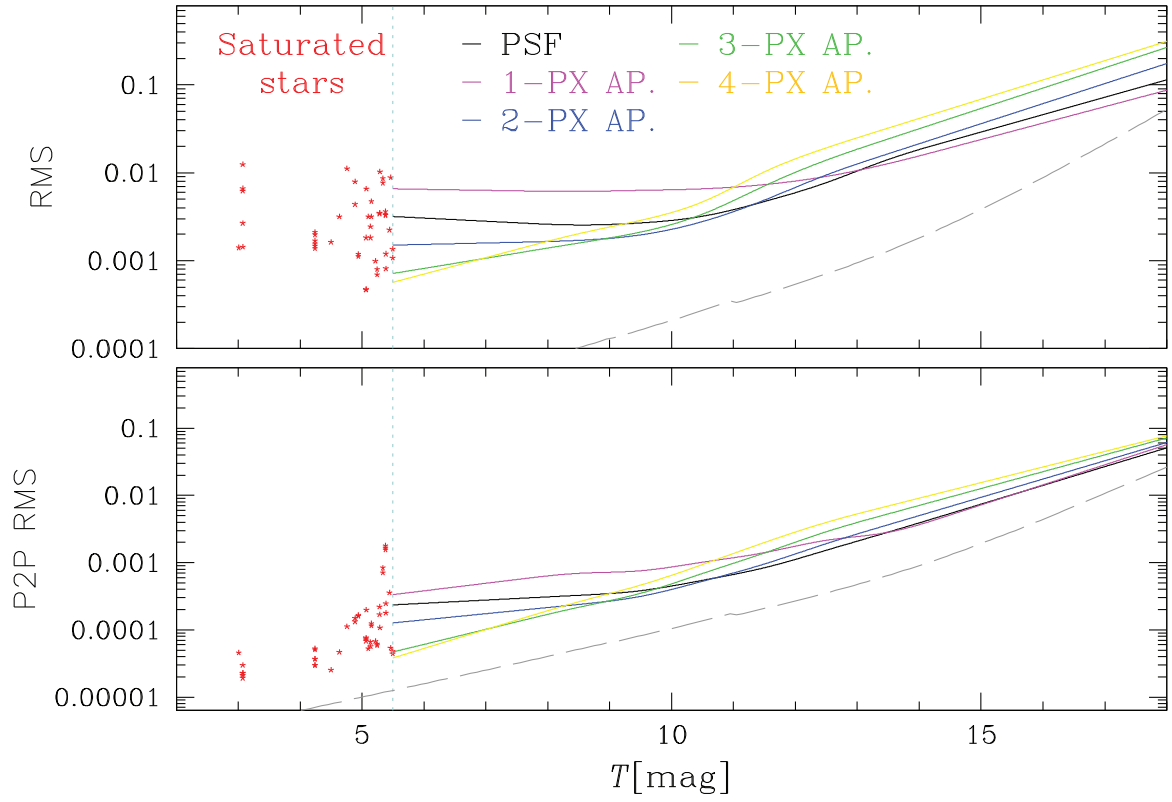

Figure 4. Photometric rms (top panel) and `P2P` rms (bottom panel) mean trends as a function of the *TESS* magnitude for all the light curves extracted in this work, colour-coded on the basis of the photometric method adopted: black for PSF-fitting photometry, and magenta, blue, green, and yellow for 1-, 2-, 3-, and 4-pixel aperture photometries, respectively. Red points represent the saturated stars. The grey dashed lines represent the theoretical limit.

light curve of the star *Gaia* DR2 5290850609994130560: In this case, we defined a knot every 13 h (grey lines in panel a).

We performed the procedure that we are going to describe considering each sector independent from the others; in a second step, we performed again the same procedure for that stars observed in more than one sector and considering the entire light curve.

For the flattened light curves, we extracted the transit-fitting least-squares (TLS) periodograms[4] (Hippke & Heller 2019), searching for transiting objects having period in the range $0.6\,\mathrm{d} \leq P \leq 0.5 \times T_{\mathrm{LC}}$, where T_{LC} is the maximum temporal baseline of the light curve (usually, for a single sector, $T_{\mathrm{LC}} \sim 27\,\mathrm{d}$). In addition to the periodograms, the routine extracted many parameters useful to discriminate between light curves with/without transit signals, such as the signal detection efficiency (SDE), the signal-to-noise ratio (SNR), the depth of the transit, and the significance between odd and even transit depths ($\sigma_{\mathrm{odd\text{-}even}}$). We used these parameters to perform a first selection of candidates: We divided the SDE and SNR distributions in intervals $\delta P = 0.5$ d, and, within each of them, we calculated their 3.5σ-clipped mean ($\bar{\mathrm{SDE}}$ and $\bar{\mathrm{SNR}}$) and standard deviation ($\sigma_{\mathrm{S\bar{D}E}}$ and $\sigma_{\mathrm{S\bar{N}R}}$). We interpolated $\bar{\mathrm{SDE}} + 3.5\sigma_{\mathrm{S\bar{D}E}}$ and $\bar{\mathrm{SNR}} + 3.5\sigma_{\mathrm{S\bar{N}R}}$ with splines, and we saved all the light curves which SDE and SNR values are above these splines, depth <10 per cent, and $\sigma_{\mathrm{odd\text{-}even}} < 2.5$. This selection procedure is shown in panels (c_1) and (c_2) of Fig. 5: Black points show all the stars for which we extracted the periodograms and that are observed in more than one sector, magenta line show the lower boundary for SNR and SDE selections, orange points show the stars that passed all the above described selections, and blue star is the candidate *Gaia* DR2 5290850609994130560. On average, the number of stars that passed these selection is ∼3 per cent of the total number of analysed light curves. After this selection, in order to avoid false positive due to blends, we identified the groups of stars which present similar period within 0.05 d and they are separated by <5 pixels, and we exclude all these stars if one of them shows a signal that can not be associated with a transiting planet (e.g. a too deep transit or the presence of a secondary eclipse). Finally, we visually inspected the remaining light curves to check the odd/even transit depths (like in panels d of Fig. 5), the presence of artefacts that generate false transits, and the presence of secondary eclipses. On average, the final list of candidate transiting object contains ∼0.1 per cent of the analysed objects; these candidates went through a detailed vetting procedure to exclude possible remaining false positives.

3.1 Vetting of the candidates

We verified that the objects that survived to the previously described selections are genuine candidates, checking if the transit signals are due to a neighbour source. In order to verify this hypothesis, we performed three different tests.

For the first test, we verified if the transit depth of the candidate object changes considering light curves obtained with different photometric methods. For example, if the transit events are due to a neighbour eclipsing binary, we expect that large photometric apertures give deeper transit events. Moreover, as already demonstrated in Paper I, PSF-fitting photometry is less affected by contamination than aperture photometry and allows us to discriminate between

[4]TLS v.1.0.24; https://github.com/hippke/tls.

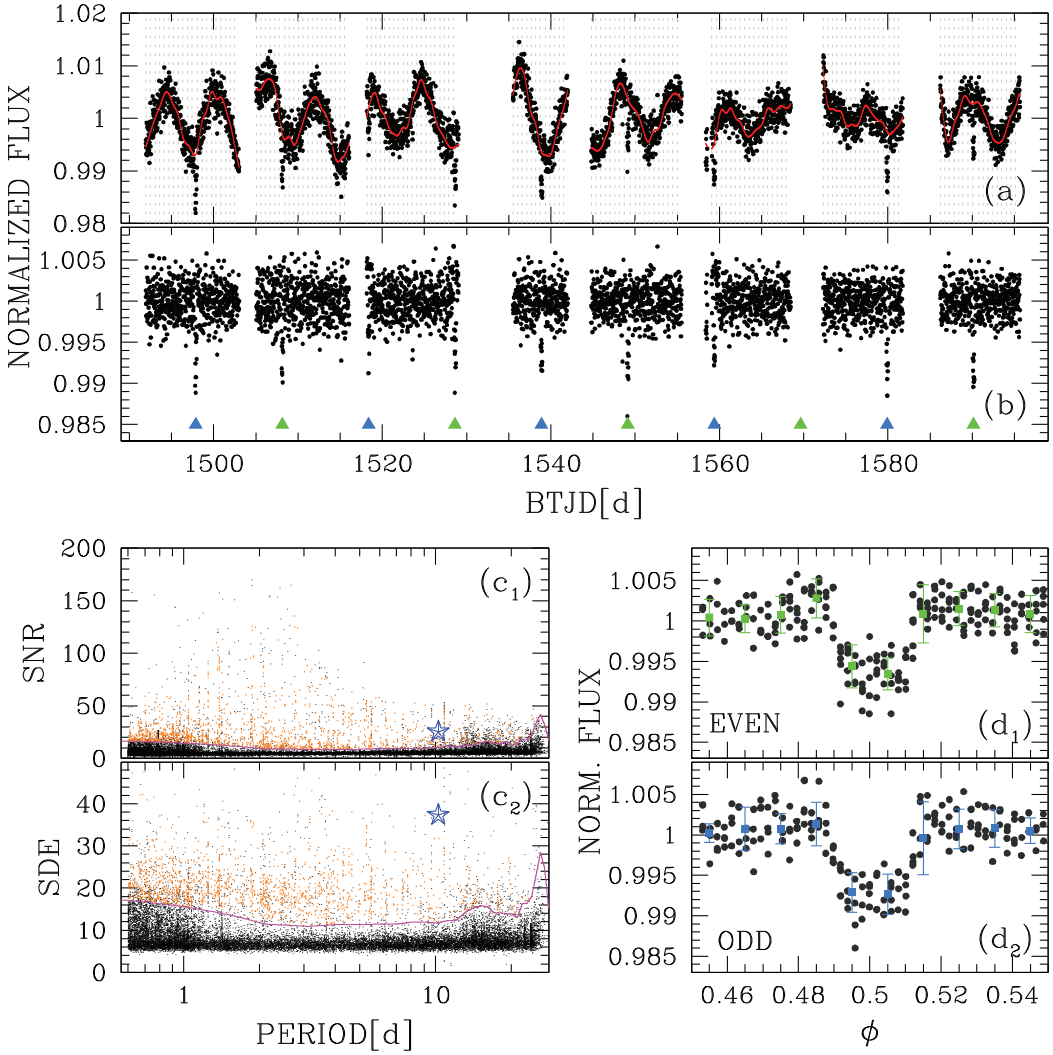

Figure 5. Overview of the successive steps of the procedure adopted to select candidate transiting objects: Panel (a) shows the normalized light curve of *Gaia* DR2 5290850609994130560 from Sectors 7 to 10. The model (in red) is obtained interpolating a fifth-order spline on a grid of knots spaced every 13 h (grey lines). Panel (b) shows the same light curve after removing the variability of the star: Azure/green arrows show the odd/even transit events, found extracting the TLS periodogram. Panels (c) illustrate the procedure of selection of stars on the basis of the parameters extracted with the TLS routine: Black points show all the stars observed in more than one sector, magenta lines show the limits above which stars pass the selection based on SDE/S/ parameters, orange points show the stars that pass all the selections (SDE/SNR/depth of transit/$\sigma_{\text{odd-even}}$), and blue star is *Gaia* DR2 5290850609994130560. Panels (d_1) and (d_2) are the phased even and odd transits, respectively. Green and azure points show the means (and their standard deviations) of the phased points calculated in bins of width 0.01. A comparison of even/odd transit depths is useful to discriminate between candidate exoplanets and eclipsing binaries (see the text for details).

true and false positives. To perform this test, we estimated the mean value (and its standard deviation σ) of the transit depth for each photometric method; if the transit associated with a photometric method is 2σ deeper than the mean transit depth associated with the analysed light curve, we considered the star as false positive.

The second test consisted in checking the binned phased light curve with a period equal to 0.5, 1, and 2 times the period found by TLS, and searching for secondary eclipses outside the primary transit. A star is considered false positive if the mean depths of even/odd transits differ by more than 2σ.

Finally, we computed the in/out-of-transit difference centroid to check if the transit events are associated to the target or to a close star. To calculate the centroid, we followed the procedure illustrated in Fig. 6 in the case of the star *Gaia* DR2 5290850609994130560: We identified the FFIs corresponding to the in-of-transit and out-of-transit points of the light curve, (light blue and light red shaded regions in the bottom right-hand panel of Fig. 6, respectively). For each transit, we calculated the mean out-of-transit image, the mean in-of-transit image, and their difference (top, middle, and bottom left-hand panels of Fig. 6, respectively). For each transit, we then calculated the photocentre on the difference image (magenta cross) and its offset relative to the *Gaia* DR2 position of the target star (yellow circle). Finally, for each sector, we calculated the mean value and its standard deviation of all the offsets. Top right-hand panel shows the finding chart (95×95 arcsec^2) based on the *Gaia* DR2 catalogue and centred on *Gaia* DR2 5290850609994130560: The average offsets for all the sectors in which the star is observed are all located at a distance $\sim$20 arcsec from the target star, in a region corresponding to two close stars of magnitude $\sim$14.5 (*Gaia* DR2 5290850609994130944 and *Gaia* DR2 5290850605693476608). Therefore, we discarded this candidate because the transit signals are not associated with

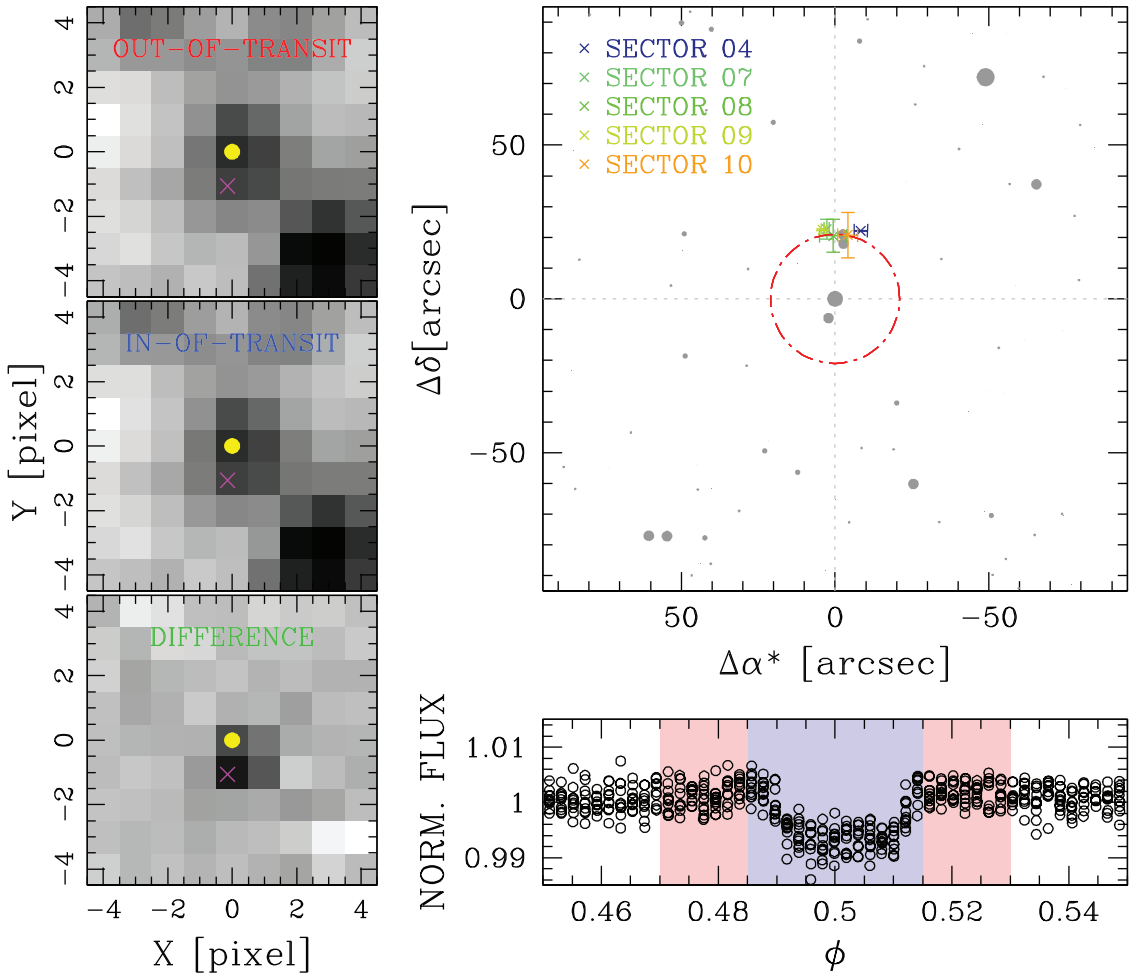

Figure 6. Vetting procedure of the candidate *Gaia* DR2 5290850609994130560 based on the position of the out-/in-of-transit difference image centroid. Left-hand panels show the average of the images corresponding to out-of-transit (top panel) and in-of-transit (middle panel) points, and the difference between these two images (bottom panel); the yellow circle shows the position of the target star as reported in the *Gaia* DR2 catalogue, while the magenta cross shows the photocentre calculated on the difference image. The top right-hand panel shows the 95 × 95 arcsec^2 finding chart centred on the target star and based on the *Gaia* DR2 catalogue. The crosses, colour-coded as in the legend, are the mean offsets calculated for each sector in which the star is observed; the red circle represents the photometric aperture adopted to analyse the light curve. The bottom right-hand panel shows the phased light curve of the target star: Light red and blue regions contain the out- and in-of-transit points, respectively.

the cluster member, but with a background star close to our target.

3.2 *TESS* Objects of Interest

We cross-matched our catalogue of analysed cluster members with the list of the *TESS* Objects of Interest[5] (TOIs) released by the *TESS* team. We found five stars in common: Three of them (TOI-496, TOI-681, and TOI-837) are also detected by our pipeline (PATHOS-6, PATHOS-25, and PATHOS-30). The other two TOIs were initially detected in the first selection of candidates we did, and then excluded by our vetting: (1) TOI-517 resulted to be an eccentric eclipsing binary with period $P \sim 9.885$ d (as also reported in the public comments of the TOI); and (2) from the analysis of the in/out-of-transit centroid of TOI-861, we found that the signal is associated with a close star (TIC 0372913432) at ∼40 arcsec from the target, and that this star is catalogued as binary by Bailey et al. (2018).

4 MODELLING OF THE TRANSITS

In our final catalogue of genuine transiting objects, there are 33 sources associated with 28 stellar clusters. For the extraction of the physical parameters (that can be obtained from a light-curve analyses) of the transiting objects, we need to know the stellar parameters. As stars in open clusters are located at the same distance and have the same chemical composition and age, we can use theoretical models to estimate their main parameters including temperature, mass, and radius. In the next section, we describe how we extracted these, which will be then used as priors for the modelling of the transits (Section 4.2).

4.1 Stellar parameters

We extracted the information on the cluster members that host candidate transiting exoplanets by fitting isochrones to the colour–

[5] https://tess.mit.edu/toi-releases/go-to-alerts/.

Table 1. Cluster parameters.

Cluster name	Age (Myr)	Distance (pc)	$E(B-V)$	π^a (mas)	Reference
Alessi 8	137 ± 35	663.7 ± 9.5	0.10 ± 0.01	1.479 ± 0.046	(2)
ASCC 85	32 ± 3	870.0 ± 5.1	0.52 ± 0.05	1.119 ± 0.085	(2)
ASCC 88	20 ± 2	883.3 ± 5.5	0.73 ± 0.07	1.097 ± 0.060	(2)
Collinder 292	498 ± 52	1461.5 ± 16.9	0.29 ± 0.01	0.528 ± 0.045	(1)
Haffner 14	195 ± 10	4359.1 ± 38.4	0.61 ± 0.01	0.226 ± 0.041	(1)
Harvard 5	65 ± 34	1203.9 ± 15.6	0.22 ± 0.01	0.764 ± 0.044	(1)
IC 2602	35 ± 2	152.3 ± 1.0	0.03 ± 0.01	6.561 ± 0.157	(1)
Melotte 101	125 ± 13	2134.7 ± 9.2	0.45 ± 0.05	0.439 ± 0.048	(2)
Muzzio 1	5 ± 4	1824.8 ± 24.3	1.02 ± 0.56	0.519 ± 0.023	(3)
NGC 2112	2065 ± 207	1103.6 ± 3.6	0.63 ± 0.06	0.877 ± 0.066	(2)
NGC 2318	560 ± 56	1342.9 ± 8.5	0.44 ± 0.04	0.716 ± 0.042	(2)
NGC 2323	95 ± 10	921.3 ± 6.8	0.15 ± 0.01	0.997 ± 0.057	(2)
NGC 2437	220 ± 22	1582.3 ± 3.9	0.15 ± 0.01	0.603 ± 0.060	(2)
NGC 2516	251 ± 5	415.1 ± 1.0	0.09 ± 0.01	2.417 ± 0.045	(1)
NGC 2527	830 ± 48	572.0 ± 5.6	0.06 ± 0.01	1.536 ± 0.070	(1)
NGC 2548	525 ± 53	758.8 ± 2.0	0.04 ± 0.01	1.289 ± 0.065	(2)
NGC 2669	82 ± 3	1124.1 ± 10.4	0.20 ± 0.01	0.845 ± 0.046	(1)
NGC 2671	338 ± 34	1396.5 ± 7.2	0.98 ± 0.10	0.687 ± 0.031	(2)
NGC 3114	200 ± 20	1017.3 ± 1.1	0.08 ± 0.01	0.954 ± 0.048	(2)
NGC 3532	399 ± 10	485.3 ± 1.0	0.02 ± 0.01	2.066 ± 0.062	(1)
NGC 5316	152 ± 5	1437.5 ± 12.6	0.25 ± 0.01	0.665 ± 0.055	(1)
NGC 5925	180 ± 18	1413.2 ± 6.2	0.75 ± 0.07	0.679 ± 0.050	(1)
Ruprecht 48	398 ± 40	3784.4 ± 79.5	0.28 ± 0.03	0.235 ± 0.038	(2)
Ruprecht 82	353 ± 47	2206.0 ± 24.5	0.33 ± 0.02	0.430 ± 0.038	(1)
Ruprecht 94	20 ± 2	2511.5 ± 29.5	0.05 ± 0.05	0.369 ± 0.031	(2)
Ruprecht 151	411 ± 25	1179.8 ± 25.2	0.19 ± 0.01	0.867 ± 0.056	(1)
SAI 91	676 ± 68	3571.6 ± 90.7	0.44 ± 0.08	0.251 ± 0.040	(2)
Trumpler 22	25 ± 15	2364.8 ± 24.1	0.59 ± 0.01	0.386 ± 0.028	(1)

References. (1) Bossini et al. (2019); (2) Kharchenko et al. (2016); (3) Bica & Bonatto (2011).
[a]Mean cluster parallax from Cantat-Gaudin et al. (2018).

magnitude diagrams (CMDs) of each stellar cluster and deriving the stellar parameters (mass, effective temperature, luminosity, and radius) interpolating colour and magnitude of each star on the isochrone. In this work, we used the last release of BaSTI ('a Bag of Stellar Tracks and Isochrones') models (Hidalgo et al. 2018) to fit isochrones on the CMDs. In order to perform this fitting, it is necessary to know the age, metallicity, distance, and reddening of the stellar clusters.

Unfortunately, metallicity measurements are not available for the large part of the stellar clusters in our sample. For this reason, we considered a constant metallicity [Fe/H] = 0.0 for all the clusters and, at the end, we added to the final error on stellar parameters the contribution of considering a wrong [Fe/H] in the isochrone fitting procedure. The corresponding uncertainty has been estimated using three different isochrones with age of 300 Myr (the average age of the studied clusters), but with metallicity [Fe/H] = −0.3, 0.0, and = +0.3, which is the range of metallicities spanned by the Galactic stellar clusters for which there are [Fe/H] measurements. We found that, for main-sequence stars with mass $0.5 < M_\star < 1.5\,M_\odot$, the mean differences on the stellar radius $R_\star$, mass $M_\star$, and effective temperature $T_{\rm eff}$ between isochrones with [Fe/H] = 0.0 and ±0.3 are ∼0.03 $R_\odot$, ∼0.05 $M_\odot$, and ∼200 K, respectively.

We extracted the information on the distance of the clusters from Cantat-Gaudin et al. (2018), while ages and reddenings are extracted from two different catalogues: For 13 stellar clusters, we used the cluster parameters and the associated errors found by Bossini et al. (2019) analysing the *Gaia* DR2 CMDs; for the other clusters, we used the information given by Kharchenko et al. (2016). In the latter catalogue, the errors on age and reddening are not given. In this case, we adopted an error equal to 10 per cent of the measurement. Muzzio 1 is the only cluster that is not present in both catalogues; for this very young cluster, we used the information given by Bica & Bonatto (2011).

Table 1 lists the cluster parameters. Thanks to isochrone fits, we were able to extract the stellar parameters of the cluster members that host candidate transiting exoplanets. These parameters were then used as priors in the phase of modelling described in the next section. Isochrone fits are shown in Figs A1–A3.

4.2 Transit modelling

For the transit modelling and analysis, we made use of PYORBIT[6] (Malavolta et al. 2016, 2018; see also, e.g. Benatti et al. 2019). The routine is a wrapper for the transit modelling code BATMAN (Kreidberg 2015) and the affine invariant Markov chain Monte Carlo (MCMC) sampler EMCEE (Foreman-Mackey et al. 2013) combined with global optimization algorithm PYDE.[7] We included in the transit model the central time of the first transit (T_0), the period (P), the impact parameter (b), the planetary-to-stellar-radius ratio ($R_{\rm p}/R_\star$), and the stellar density ($\rho_\star$). For the modelling, we adopted a Keplerian orbit with null eccentricity. In Table 2, we listed the priors used for the fit. We used the $T_{\rm eff}$ and log (g) values obtained with isochrones fitting to extract, through a bilinear interpolation,

[6]https://github.com/LucaMalavolta/PyORBIT.
[7]https://github.com/hpparvi/PyDE.

Table 2. Star parameters and priors for the modelling.

TIC	PATHOS	Cluster	α (°)	δ (°)	π (mas)	T (mag)	$R_\star$ ($R_\odot$)	$M_\star$ ($M_\odot$)	$\rho_\star$ ($\rho_\odot$)	Period (d)	T_0 (BTJD)	LD_{c1}	LD_{c2}
0030654608	2	Muzzio 1	134.3845	−47.8477	0.5191	10.4	10.0 ± 2.00	17.0 ± 2.00	$\mathcal{N}(0.01, 0.10)$	$\mathcal{U}(2.0, 3.0)$	$\mathcal{U}(1519.0, 1520.0)$	$\mathcal{N}(0.10, 0.50)$	$\mathcal{N}(0.10, 0.50)$
0039291805	3	NGC 2112	88.7164	−0.0484	0.8964	15.2	1.12 ± 0.03	1.13 ± 0.05	$\mathcal{N}(0.80, 0.10)$	$\mathcal{U}(7.0, 7.5)$	$\mathcal{U}(1468.9, 1469.2)$	$\mathcal{N}(0.31, 0.05)$	$\mathcal{N}(0.29, 0.05)$
0042524156	4	ASCC 88	256.8882	−35.5036	1.1502	10.5	2.94 ± 0.03	5.18 ± 0.05	$\mathcal{N}(0.20, 0.10)$	$\mathcal{U}(9.8, 10.2)$	$\mathcal{U}(1631.0, 1632.0)$	$\mathcal{N}(0.15, 0.13)$	$\mathcal{N}(0.15, 0.13)$
0080317933	5	Collinder 292	237.9156	−57.2797	0.6320	12.9	1.83 ± 0.03	1.91 ± 0.05	$\mathcal{N}(0.32, 0.10)$	$\mathcal{U}(3.0, 3.5)$	$\mathcal{U}(1625.0, 1626.0)$	$\mathcal{N}(0.19, 0.05)$	$\mathcal{N}(0.23, 0.05)$
0088977253	6	NGC 2548	123.0977	−5.7687	1.2358	12.3	1.42 ± 0.03	1.42 ± 0.05	$\mathcal{N}(0.49, 0.10)$	$\mathcal{U}(2.5, 3.0)$	$\mathcal{U}(1492.0, 1493.0)$	$\mathcal{N}(0.27, 0.05)$	$\mathcal{N}(0.28, 0.05)$
0092835691	7	SAI 91	129.1193	−50.1497	0.2347	14.6	2.24 ± 0.05	2.02 ± 0.07	$\mathcal{N}(0.18, 0.10)$	$\mathcal{U}(22.0, 23.0)$	$\mathcal{U}(1527.0, 1528.0)$	$\mathcal{N}(0.19, 0.05)$	$\mathcal{N}(0.23, 0.05)$
0094589619	8	NGC 2437	115.7338	−14.5810	0.6238	13.8	1.46 ± 0.03	1.55 ± 0.05	$\mathcal{N}(0.49, 0.10)$	$\mathcal{U}(11.8, 12.5)$	$\mathcal{U}(1496.0, 1497.0)$	$\mathcal{N}(0.24, 0.05)$	$\mathcal{N}(0.26, 0.05)$
0125414447	9	NGC 2323	105.7303	−8.4369	0.9320	14.2	1.00 ± 0.03	1.10 ± 0.05	$\mathcal{N}(1.10, 0.10)$	$\mathcal{U}(3.5, 4.0)$	$\mathcal{U}(1493.0, 1494.0)$	$\mathcal{N}(0.32, 0.05)$	$\mathcal{N}(0.30, 0.05)$
0126600730	10	Haffner 14	116.0772	−28.3253	0.2145	15.4	2.11 ± 0.03	2.56 ± 0.05	$\mathcal{N}(0.27, 0.10)$	$\mathcal{U}(6.0, 6.5)$	$\mathcal{U}(1497.0, 1498.0)$	$\mathcal{N}(0.15, 0.05)$	$\mathcal{N}(0.20, 0.05)$
0144995073	11	NGC 2669	131.4641	−52.9284	0.8289	13.7	1.36 ± 0.03	1.41 ± 0.05	$\mathcal{N}(0.55, 0.10)$	$\mathcal{U}(19.5, 20.5)$	$\mathcal{U}(1518.5, 1519.5)$	$\mathcal{N}(0.27, 0.05)$	$\mathcal{N}(0.28, 0.05)$
0147069011	12	Alessi 8	232.8684	−51.1783	1.5017	12.5	1.25 ± 0.03	1.30 ± 0.05	$\mathcal{N}(0.66, 0.10)$	$\mathcal{U}(7.0, 7.5)$	$\mathcal{U}(1628.0, 1629.0)$	$\mathcal{N}(0.28, 0.05)$	$\mathcal{N}(0.29, 0.05)$
0147426828	13	NGC 2318	104.8768	−13.2535	0.6934	14.1	1.49 ± 0.03	1.49 ± 0.05	$\mathcal{N}(0.45, 0.10)$	$\mathcal{U}(1.0, 1.7)$	$\mathcal{U}(1492.0, 1493.0)$	$\mathcal{N}(0.25, 0.05)$	$\mathcal{N}(0.27, 0.05)$
0153734545	14	NGC 2527	121.2402	−28.1462	1.5019	9.9	2.72 ± 0.03	2.05 ± 0.05	$\mathcal{N}(0.11, 0.10)$	$\mathcal{U}(3.0, 3.5)$	$\mathcal{U}(1493.0, 1494.0)$	$\mathcal{N}(0.22, 0.05)$	$\mathcal{N}(0.25, 0.05)$
0153735144	15	NGC 2527	121.1537	−28.2948	1.5432	11.6	1.51 ± 0.03	1.46 ± 0.05	$\mathcal{N}(0.43, 0.10)$	$\mathcal{U}(3.2, 4.0)$	$\mathcal{U}(1493.0, 1494.0)$	$\mathcal{N}(0.26, 0.05)$	$\mathcal{N}(0.27, 0.05)$
0159059181	16	NGC 2112	88.3711	+0.4239	0.8356	14.2	1.52 ± 0.03	1.33 ± 0.05	$\mathcal{N}(0.38, 0.10)$	$\mathcal{U}(5.0, 5.5)$	$\mathcal{U}(1470.9, 1471.4)$	$\mathcal{N}(0.28, 0.05)$	$\mathcal{N}(0.28, 0.05)$
0181602717	17	NGC 2671	131.7366	−41.9773	0.5930	15.2	1.47 ± 0.03	1.53 ± 0.05	$\mathcal{N}(0.48, 0.10)$	$\mathcal{U}(2.0, 2.7)$	$\mathcal{U}(1517.0, 1518.0)$	$\mathcal{N}(0.24, 0.05)$	$\mathcal{N}(0.25, 0.05)$
0236084210	18	ASCC 85	251.5388	−45.3214	1.1433	11.5	1.84 ± 0.03	2.66 ± 0.05	$\mathcal{N}(0.42, 0.10)$	$\mathcal{U}(5.0, 5.5)$	$\mathcal{U}(1631.5, 1632.5)$	$\mathcal{N}(0.15, 0.05)$	$\mathcal{N}(0.18, 0.05)$
0300362600	19	NGC 5316	208.3975	−62.0764	0.6984	12.2	2.14 ± 0.03	2.70 ± 0.05	$\mathcal{N}(0.28, 0.10)$	$\mathcal{U}(11.0, 12.0)$	$\mathcal{U}(1601.9, 1602.5)$	$\mathcal{N}(0.15, 0.05)$	$\mathcal{N}(0.19, 0.05)$
0306385801	20	NGC 3532	166.6553	−58.8608	2.0510	9.5	2.22 ± 0.03	2.29 ± 0.05	$\mathcal{N}(0.21, 0.10)$	$\mathcal{U}(13.8, 14.5)$	$\mathcal{U}(1574.8, 1575.3)$	$\mathcal{N}(0.16, 0.05)$	$\mathcal{N}(0.21, 0.05)$
0308538095	21	NGC 2516	120.8514	−60.6655	2.4333	11.6	1.29 ± 0.03	1.32 ± 0.05	$\mathcal{N}(0.62, 0.10)$	$\mathcal{U}(11.0, 12.5)$	$\mathcal{U}(1420.0, 1421.0)$	$\mathcal{N}(0.29, 0.05)$	$\mathcal{N}(0.29, 0.05)$
0317536999	22	Ruprecht 94	172.5414	−63.1323	0.3921	14.1	1.86 ± 0.03	2.76 ± 0.05	$\mathcal{N}(0.43, 0.10)$	$\mathcal{U}(5.5, 6.0)$	$\mathcal{U}(1575.5, 1576.5)$	$\mathcal{N}(0.15, 0.05)$	$\mathcal{N}(0.17, 0.05)$
0372913337	23	NGC 2516	119.4918	−60.8459	2.3454	8.9	2.49 ± 0.03	2.74 ± 0.05	$\mathcal{N}(0.18, 0.10)$	$\mathcal{U}(1.5, 2.0)$	$\mathcal{U}(1325.0, 1326.0)$	$\mathcal{N}(0.15, 0.05)$	$\mathcal{N}(0.19, 0.05)$
0389927567	24	Melotte 101	160.2669	−65.5215	0.4321	13.0	2.26 ± 0.03	2.95 ± 0.05	$\mathcal{N}(0.25, 0.10)$	$\mathcal{U}(6.5, 7.0)$	$\mathcal{U}(1575.0, 1576.0)$	$\mathcal{N}(0.15, 0.05)$	$\mathcal{N}(0.17, 0.05)$
0410450228	25	NGC 2516	117.8949	−60.4124	2.3447	10.6	1.51 ± 0.03	1.67 ± 0.05	$\mathcal{N}(0.48, 0.10)$	$\mathcal{U}(15.5, 16.0)$	$\mathcal{U}(1420.0, 1421.0)$	$\mathcal{N}(0.22, 0.05)$	$\mathcal{N}(0.25, 0.05)$
0413809436	26	NGC 5925	232.0979	−54.5586	0.6814	14.1	1.59 ± 0.03	1.88 ± 0.05	$\mathcal{N}(0.47, 0.10)$	$\mathcal{U}(2.5, 3.0)$	$\mathcal{U}(1627.0, 1628.0)$	$\mathcal{N}(0.18, 0.05)$	$\mathcal{N}(0.23, 0.05)$
0419091401	27	Ruprecht 48	120.6352	−31.9951	0.2379	13.7	3.40 ± 0.20	2.71 ± 0.10	$\mathcal{N}(0.07, 0.10)$	$\mathcal{U}(12.5, 13.0)$	$\mathcal{U}(1499.0, 1500.0)$	$\mathcal{N}(0.15, 0.10)$	$\mathcal{N}(0.21, 0.10)$
0432564189	28	Ruprecht 82	146.5229	−53.9787	0.4632	13.6	2.12 ± 0.05	2.28 ± 0.05	$\mathcal{N}(0.23, 0.10)$	$\mathcal{U}(3.5, 4.0)$	$\mathcal{U}(1546.0, 1547.0)$	$\mathcal{N}(0.16, 0.05)$	$\mathcal{N}(0.21, 0.05)$
0450610413	29	Harvard 5	186.7427	−60.6906	0.6932	12.2	1.72 ± 0.05	2.30 ± 0.05	$\mathcal{N}(0.45, 0.10)$	$\mathcal{U}(10.0, 11.0)$	$\mathcal{U}(1599.8, 1600.8)$	$\mathcal{N}(0.15, 0.05)$	$\mathcal{N}(0.20, 0.05)$
0460205581	30	IC 2602	157.0373	−64.5052	6.9893	9.9	1.07 ± 0.03	1.15 ± 0.05	$\mathcal{N}(0.93, 0.10)$	$\mathcal{U}(8.0, 8.5)$	$\mathcal{U}(1574.0, 1575.0)$	$\mathcal{N}(0.31, 0.05)$	$\mathcal{N}(0.30, 0.05)$
0460950389	31	IC 2602	159.1580	−64.7982	6.6229	11.6	0.84 ± 0.03	0.81 ± 0.05	$\mathcal{N}(1.37, 0.10)$	$\mathcal{U}(2.5, 3.0)$	$\mathcal{U}(1572.0, 1573.0)$	$\mathcal{N}(0.43, 0.05)$	$\mathcal{N}(0.38, 0.05)$
0462004618	32	NGC 3114	149.9120	−59.9032	1.0387	11.3	2.01 ± 0.03	2.43 ± 0.05	$\mathcal{N}(0.29, 0.10)$	$\mathcal{U}(2.0, 2.5)$	$\mathcal{U}(1544.0, 1545.0)$	$\mathcal{N}(0.15, 0.05)$	$\mathcal{N}(0.20, 0.05)$
0748919024	33	Ruprecht 151	115.1315	−16.3216	0.7387	13.4	1.46 ± 0.03	1.49 ± 0.05	$\mathcal{N}(0.48, 0.10)$	$\mathcal{U}(2.0, 3.0)$	$\mathcal{U}(1493.8, 1494.5)$	$\mathcal{N}(0.25, 0.05)$	$\mathcal{N}(0.27, 0.05)$
1036769612	34	Trumpler 22	217.5064	−61.3249	0.4244	15.8	1.43 ± 0.05	1.58 ± 0.10	$\mathcal{N}(0.54, 0.20)$	$\mathcal{U}(7.1, 7.7)$	$\mathcal{U}(1599.0, 1600.0)$	$\mathcal{N}(0.24, 0.05)$	$\mathcal{N}(0.27, 0.05)$

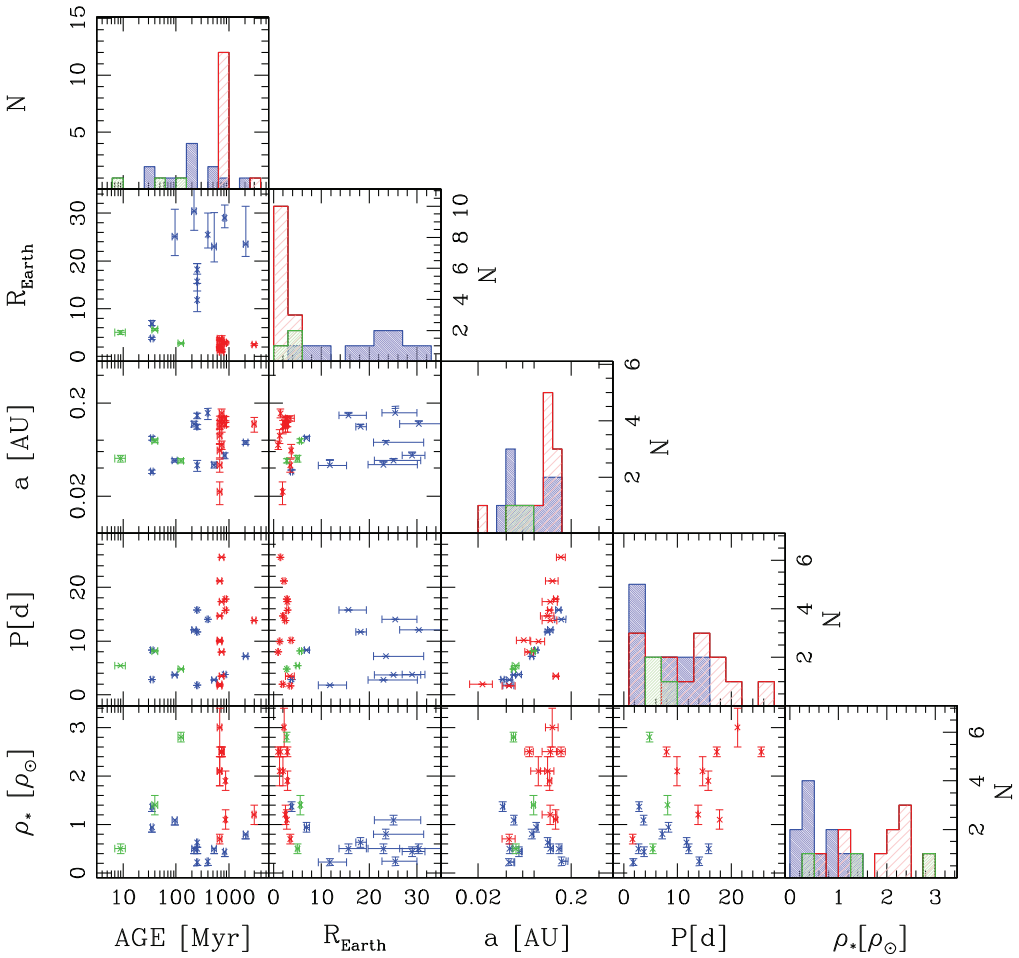

Figure 7. Correlations between the cluster, stellar, and exoplanets properties. Blue points and histograms show the results of this work; red points and histograms show the results obtained using data of open clusters collected by *Kepler*; and green points and histograms represent stars in associations.

the priors on the limb darkening (LD) coefficients from the grid of values published by Claret (2018); for the modelling, we adopted the LD parametrization used by Kipping (2013). In the modelling process, we took into account of the 30-min cadence of the *TESS* time-series (Kipping 2010). The routine explored all the parameters in linear space. For our fit, we made use of a number of walkers $N_{\rm walkers} = 110$, equal to 10 times the number of free parameters. We ran, for each model, the sampler for 50 000 steps, removing the first 15 000 steps as burn-in and using a thinning factor of 100.

Appendix A shows all results: In Table A1 are listed the outputs of our fit and the clusters associated with each transiting object of interest; Figs A1–A3 show, for each transiting object, the position of the star on the *Gaia* DR2 CMD of the cluster to which it is associated (left-hand panel), the folded light curve with the overimposed model of the transit (top right-hand panel), the difference between the observed points and the model (middle right-hand panel), the finding chart and the vector-point diagram of the target, and its surrounding sources from the *Gaia* DR2 catalogue (bottom right-hand panels).

5 EXOPLANETS IN OPEN CLUSTERS: RESULTS

From our data set, we extracted 33 objects of interest whose light curves show transit signals. In this section, we isolate the more significant candidate exoplanets and compare the candidate exoplanets and cluster parameters.

From our final list, we excluded all stars that host candidate planets with a radius $R_{\rm P} \geq 3.0\,R_{\rm J}$ (15 objects) because of their doubtful planet nature. We also excluded all those stars that have a parallax that differs $>3\sigma$ from the mean parallax of the cluster (see Table 1), stars that are not located on the main sequence in the CMD of the cluster (i.e. $>2\sigma$ from the mean colour of the main sequence), and stars whose proper motion differs $>4\sigma$ from the mean proper motion of the cluster. In this way, we were left with 11 candidates (PATHOS-3, 6, 8, 9, 15, 20, 21, 23, 25, 30, and 31) in eight open clusters, with seven of them (NGC 2112, NGC 2437, NGC 2516, NGC 2527, NGC 2548, NGC 3532, and IC 2602) having a solar metallicity (Netopil et al. 2016), while for NGC 2323, there are no metallicity measurements; nine of these candidate exoplanets orbit stars with radii $R_\star \lesssim 1.5\,R_\odot$, while PATHOS-20 and PATHOS-23 orbit stars with $R_\star \sim 2.2$ and $\sim 2.5\,R_\odot$, respectively.

Fig. 7 shows the correlations between cluster age and stellar density and some candidate exoplanet parameters, like period, semimajor axis, and radius. In this analysis, we also included the candidate and confirmed transiting exoplanets in open clusters and young association found by *Kepler*/*K2* and *TESS*, present in literature. In particular, we considered the first two discovered exoplanets (Kepler-66b and Kepler-67b; Meibom et al. 2013) in NGC 6811 (∼863 Myr); the four exoplanets K2-25b, K2-136Ab,

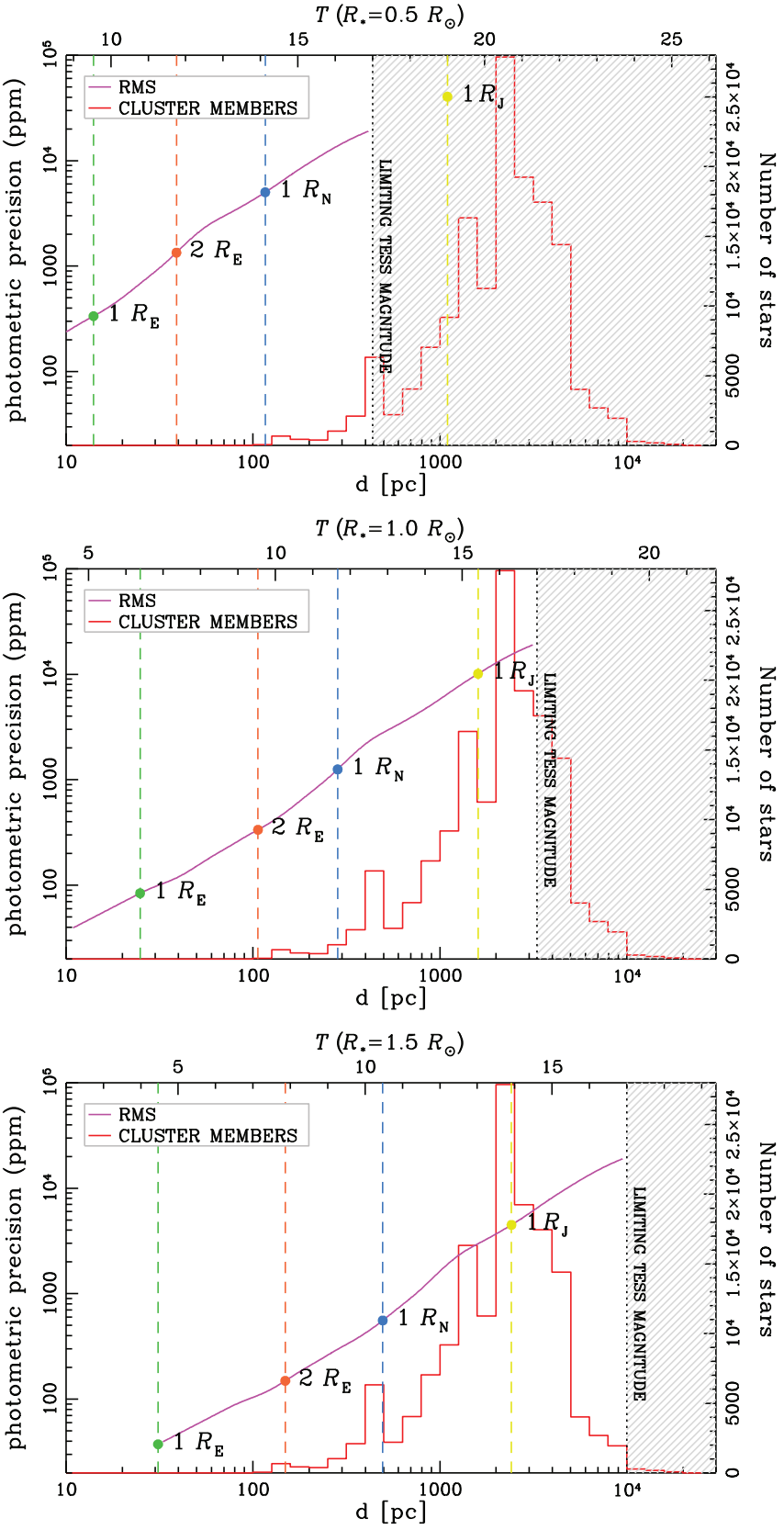

Figure 8. Detectability limits of transits of exoplanets of size $R_P = 1\ R_E$ (green dot), $2\ R_E$ (orange dot), $1\ R_N$ (light blue dot), and $1\ R_J$ (yellow dot) orbiting stars with radius $R_\star = 0.5$ (top panel), 1.0 (middle panel), and $1.5\ R_\odot$ (bottom panel). The magenta line represents the average rms distribution as a function of the magnitude obtained from flattened light curves. The red histogram shows the distance distribution of the cluster members studied in this work. The grey zone represents the range of magnitudes outside the range of detection of *TESS*. The upper axis of each panel gives the apparent magnitude of a star with $R_\star = X\ R_\odot$, with $X = 0.5,\ 1.0,\ 1.5$, at the corresponding distance of the lower axis.

c, and d (Ciardi et al. 2018; Mann et al. 2018) in the Hyades (∼730 Myr); the six exoplanets in M 44 (∼670 Myr), e.g. K2-95b, K2-100b, K2-101b, K2-102b, K2-103b, and K2-104b (Barros et al. 2016; Libralato et al. 2016b; Obermeier et al. 2016; Pope et al. 2016; Mann et al. 2017; Pepper et al. 2017); and the Ruprecht 147 (∼3 Gyr) member K2-213b (Curtis et al. 2018). In our analysis, we also considered the exoplanets K2-33b in the young association Upper Scorpius (∼10 Myr; David et al. 2016b; Mann et al. 2016b), EPIC 247267267 b in the Cas-Tau group (∼120 Myr; David et al. 2018) and the recently discovered exoplanets DS Tuc Ab (Benatti et al. 2019; Newton et al. 2019), discovered by *TESS* and members of the Tucana–Horologium young association (∼40 Myr).

Blue points and histograms in Fig. 7 correspond to the objects identified in this work; red points and histograms show the planets from *Kepler* observations; and green points and histograms represent stars in young associations. Considering all the points, there is no evident correlations among cluster/stellar and (candidate) exoplanet parameters. Fig. 7 illustrates the difference between the type of exoplanets in stellar clusters detected by *Kepler* and *TESS*: The large part of the candidates found in this work are Jupiter-size objects orbiting stars with $0.7 \lesssim R_\star \lesssim 2.5\,R_\odot$, while the transiting objects found with *Kepler* and *K2* data of open clusters are Neptune- and Earth-size exoplanets hosted by $R_\star \lesssim 1\,R_\odot$ stars. This is mainly due to the combination of two observational biases: (i) *Kepler* data limiting magnitude is about 2–3 mag fainter than the*TESS* one, and, therefore, at a given magnitude, *Kepler* photometric precision is higher than *TESS* one, allowing us to find smaller exoplanets around fainter main-sequence stars; and (ii) three of the four open clusters (Hyades, M 44, and Ruprecht 147) observed by *Kepler* and whose members host known exoplanets are 'close' clusters ($d \lesssim 300$ pc, while NGC 6811 is at ∼1250 pc), while distances of the open clusters studied in this work are between 100 pc and 15 kpc, with 50 per cent of the open cluster having $d \gtrsim 3$ kpc.

Fig. 8 shows how the distance of the open clusters affects our results. We analysed what kind of planets we are able to detect in the light curves of stars having a radius $R_\star = 0.5$ (top panel), 1.0 (middle panel), and $1.5\,R_\odot$ (bottom panel), and located at distances between 10 and 15 000 pc. Using isochrones, we calculated the average absolute *TESS* magnitude of these stars and then we calculated their apparent magnitudes for different distances. The upper axis of each panel illustrates the apparent magnitude T of a star at the corresponding distance of the lower axis. The grey zone represents the magnitude range out of reach of *TESS*. Red histogram shows the distribution of the distances of the stars in the clusters studied in this work: The peak of the distribution is at $d \sim 3000$ pc. Magenta line represents the mean distribution of the rms calculated using all the analysed flattened light curves; the rms gives us an idea about the detectability of an exoplanet of radius R_p hosted by a star of radius $R_\star$ located at distance d.

We analysed four different types of exoplanets orbiting stars into the three $R_\star$ groups: Earth-size planet ($R_\mathrm{p} = 1\,R_\mathrm{E}$, green dot in Fig. 8), super-Earth-size planet ($R_\mathrm{p} = 2\,R_\mathrm{E}$, orange dot in Fig. 8), Neptune-size planet ($R_\mathrm{p} = 1\,R_\mathrm{N}$, light blue dot in Fig. 8), and Jupiter-size planet ($R_\mathrm{p} = 1\,R_\mathrm{J}$, yellow dot in Fig. 8). We calculated the expected photometric decrement in the light curve $\delta_\mathrm{phot} = (R_\mathrm{P}/R_\star)^2$ due to the exoplanet transit and, by using the photometric precision distribution, we calculated the maximum distance at which the transit of a planet of radius R_P is still detectable (at 1σ) in the light curve of a star with radius $R_\star$. Finally, we used this distance, combined with the CMD M_T versus $(G_\mathrm{BP} - G_\mathrm{RP})_0$, to extract the number ($N_\star$) of cluster members having radius $R_\star$ for

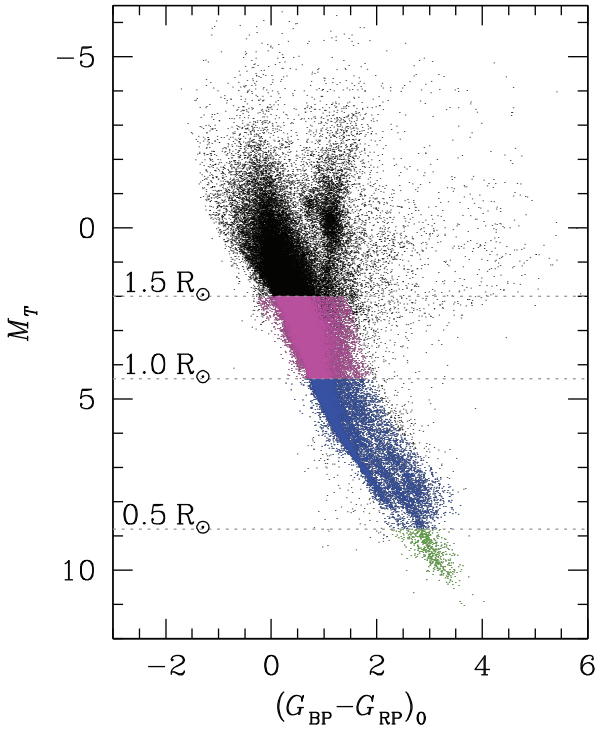

Figure 9. The M_T versus $(G_\mathrm{BP} - G_\mathrm{RP})_0$ CMD for the analysed stars in this work. Green, blue, and magenta points show the main-sequence stars in the radius intervals $R_\star \lesssim 0.5\,R_\odot$, $0.5 \lesssim R_\star \lesssim 1.0\,R_\odot$, and $1.0 \lesssim R_\star \lesssim 1.5\,R_\odot$, respectively.

which this kind of transits can be detected in their light curves. This CMD is shown in Fig. 9. For the reddening correction, we used the tridimensional extinction map of Lallement et al. (2018) in conjunction with Bailer-Jones et al. (2018) distances to estimate the amount of interstellar reddening to the target stars. We evaluated the reddening $E(B - V)$ on a sample of N equally spaced nodal points along each target direction by considering the weighted average of the 27 surrounding voxels reddening ($3 \times 3 \times 3$ voxels cube around the nodal point). The reddening was weighted by the distance of the nodal point from each one of the neighbouring voxels' centres while the distance between two adjacent nodal points was 2 pc. We therefore summed up the reddening along the boresight to derive the integrated reddening to the target stars. For stars falling outside the map, we added a correction to account for the extinction from the edge of the map to the target position. The correction was calculated using the dust model described in Binney et al. (2014). The entire procedure will be further described in Montalto et al. (in preparation). For each cluster, we calculated the 3.5σ-clipped mean $E(B - V)$ value and used the equations reported by Stassun et al. (2019) to correct the colours and the magnitudes of the stars.

We selected the main-sequence stars as follows: first, we excluded the evolved stars of each open cluster visually inspecting each CMD. In the second step, we determined the fiducial line of all the main-sequence stars by using the naive estimator (Silverman 1986, see Nardiello et al. 2015b for a detailed description of the method), and we selected all the stars whose colours are within $2\,\sigma$ from the mean colour of the fiducial line. Green, blue, and magenta points in Fig. 9 show the main-sequence stars with radii $R_\star \lesssim 0.5\,R_\odot$, $0.5 \lesssim R_\star \lesssim 1.0\,R_\odot$, and $1.0 \lesssim R_\star \lesssim 1.5\,R_\odot$, respectively, and will be used in the following analysis.

The three panels of Fig. 8 show that we are not able to detect transiting exoplanets with $R_P \leq 1\ R_E$ around cluster members with $R_\star \gtrsim 0.5\,R_\odot$: Indeed, in order to be able to detect this kind of exoplanets, it would be necessary that the hosting star is at a distance $d \lesssim 30$ pc, but no open cluster studied in this work satisfies this condition. In the case of super-Earths ($R_P \lesssim 2\ R_E$), we have no possibility to find them around cluster members with $R_\star < 0.5\,R_\odot$, but we are able to detect this kind of exoplanet in the light curves of stars with $0.5 \lesssim R_\star \lesssim 1.5\,R_\odot$ and located at $d \lesssim 150$ pc. For the two intervals of stellar radii $0.5 \lesssim R_\star \lesssim 1.0\,R_\odot$ and $1.0 \lesssim R_\star \lesssim 1.5\,R_\odot$, from the CMD of Fig. 9 combined with information on the distance from Fig. 8, we extracted a total of $N_\star = 23 \pm 5$ and 20 ± 4 stars with these radii, respectively. In our survey, we detected no super-Earth transits. This result is in agreement with the frequency of field exoplanets from the *Kepler* survey, as tabulated by Fressin et al. (2013).

Following Curtis et al. (2018), we also calculated the number of expected transiting super-Earths in our sample, by using the equation

$$N_{\rm planet} = N_\star \times f_\star \times {\rm Pr}_{\rm transit}, \quad (2)$$

where $f_\star = 4.82$ per cent is the percentage of stars with at least one exoplanet for the period range 0.8–10 d estimated by Fressin et al. (2013), ${\rm Pr}_{\rm transit} \simeq R_\star/a$ is the transit probability, and a is calculated assuming an average period $P = 10$ d. The result of this estimate is $N_{\rm planet} \simeq 0$ for stars with $R_\star = 1.0$ and $1.5\,R_\odot$, consistent with our null detection.

From Figs 8 and 9, transiting exoplanets having a radius $R_P \sim 1\ R_N$ and orbiting stars with $R_\star \lesssim 0.5\,R_\odot$ can be detected in the light curve of $N_\star = 23 \pm 5$ stars. Fressin et al. (2013) estimated that $f_\star = 2.61$ per cent of field stars host Neptune-size exoplanets with periods <10 d. Correspondingly, we expect a null detection (0.02 planets) of Neptune-size exoplanets transiting low-mass main-sequence stars that are members of the studied clusters.

In the case, the hosting star has radii $0.5 \lesssim R_\star \lesssim 1.0\,R_\odot$ and $1.0 \lesssim R_\star \lesssim 1.5\,R_\odot$, and we are able to detect Neptune-size transits in the light curves of $N_\star = 1086 \pm 33$ and 1868 ± 43 stars. We found one Neptune-size exoplanet around a $R_\star \sim 1.1\,R_\odot$ star (PATHOS-30), while PATHOS-31 is a candidate Neptune orbiting a $R_\star \sim 0.8\,R_\odot$ star. By using this information, we calculated the frequency of transiting Neptune exoplanets for stars with $0.5 \lesssim R_\star \lesssim 1.5\,R_\odot$, $f_\star$, from equation (2). We found that for $0.5 \lesssim R_\star \lesssim 1.0\,R_\odot$, $f_\star = 1.84 \pm 1.84$ per cent, while for $1.0 \lesssim R_\star \lesssim 1.5\,R_\odot$, we obtained $f_\star = 0.67 \pm 0.67$ per cent; if we consider all the stars with $R \lesssim 1.5\,R_\odot$, we have a frequency of transiting Neptunes $f_\star = 1.34 \pm 0.95$ per cent, in agreement with Fressin et al. (2013), who found. $f_\star = 2.61 \pm 0.18$ per cent, within $\sim 1\sigma$.

In our survey, Jupiter-size exoplanets orbiting stars of radius $R_\star \lesssim 0.5\,R_\odot$ can be detected in the light curves of $N_\star = 544 \pm 23$ cluster members, while for stars with $0.5 \lesssim R_\star \lesssim 1.0\,R_\odot$ and $1.0 \lesssim R_\star \lesssim 1.5\,R_\odot$, we were able to detect transits of this kind of exoplanets in the light curves of $N_\star = 17\,583 \pm 133$ and $26\,776 \pm 164$ cluster stars, respectively. We did not detect any Jupiter-size exoplanet around stars with $R_\star \lesssim 0.5\,R_\odot$; it is expected assuming a frequency of giant planets ($\sim$0.43 per cent) as in Fressin et al. (2013). We calculated the observed frequency of transiting Jupiters in the other two ranges of stellar radii, following the procedure already adopted for Neptune-size planets. We found one giant exoplanet orbiting $0.5 \lesssim R_\star \lesssim 1.0\,R_\odot$, with a corresponding frequency $f_\star = 0.11 \pm 0.11$ per cent; six Jupiter-size exoplanets were detected for stars with radii $1.0 \lesssim R_\star \lesssim 1.5\,R_\odot$, with a frequency of $f_\star = 0.28 \pm 0.11$ per cent. Considering all the stars with $R_\star \lesssim 1.5\,R_\odot$ for which we are able to detect Jupiter-size transiting exoplanets, we obtain a frequency $f_\star = 0.19 \pm 0.07$ per cent, which is significantly lower than that found by Fressin et al. (2013, $f_\star = (0.43 \pm 0.05)$ per cent).

We want to emphasize that, in the statistical analysis we performed, there two effects that partially compensate each other and that can affect our estimated frequencies: (i) Our detection method might miss some transit, i.e. the sample of detected candidate exoplanets might be not complete. Including the completeness correction might result in a higher value of $f_\star$. (ii) Though we applied a validation check to our targets, we could not identify all false positives, estimated to be $\sim$40 per cent by Sullivan et al. (2015) and $\sim$33 per cent by Cloutier (2019). Because of our false-positive check, the fraction of false positives in our sample is surely smaller, but not null, and this fact would decrease $f_\star$.

6 SUMMARY AND CONCLUSION

In the second work of our project PATHOS, we applied our PSF-based approach to *TESS* FFIs in order to extract high-precision light curves of stars that belong to open clusters observed by *TESS* during the first year of its mission (Sectors 1–13). We extracted and analysed 219 256 light curves of 162 901 stars located in 645 open clusters (51 475 stars are observed in more than one *TESS* sector). These open clusters span a wide range of ages (from few tens Myr up to $\sim$3 Gyr) and distances ($\sim$100–10^4 pc), allowing us to probe stars born at different times and in different environmental conditions. The light curves will be publicly available as HLSP on the PATHOS project webpage[8] (DOI: 10.17909/t9-es7m-vw14) of the MAST archive.

We searched for transit signals among the extracted and corrected light curves and, after a series of vetting tests, we isolated 33 transiting objects of interest. We extracted the physical parameters of these objects modelling the transits, and using these information combined with the stellar properties, we selected 11 candidate exoplanets orbiting stars of eight open clusters. One of the youngest open clusters in our sample, IC 2602 ($\sim$35 Myr), hosts two stars with candidate Neptune-size exoplanets, while in the 250-Myr-old open cluster NGC 2516, we found two warm and one hot Jupiter candidates. In the remaining clusters, we detected one transiting candidate exoplanet in each of them: NGC 2112 ($\sim$2 Gyr), NGC 2323 ($\sim$100 Myr), NGC 2437 ($\sim$220 Myr), NGC 2527 ($\sim$830 Myr), NGC 2548 ($\sim$500 Myr), and NGC 3532 ($\sim$400 Myr)

We also show that the planet detection is strongly affected by the bias due to the distance of the open clusters. Comparing the mean distribution of the photometric precision with the expected depth of the transits due to exoplanets with different radii and the percentage of stars that host different size exoplanets tabulated by Fressin et al. (2013), we expected a null detection of Earth and super-Earth size exoplanets in the light curves of the members of the open clusters analysed in this work.

We detected two Neptune-size candidate exoplanets around two IC 2602 members with radii $R_\star \lesssim 1.5\,R_\odot$; consequently, we estimated that the frequency of this kind of exoplanets is $f_\star = 1.34 \pm 0.95$, consistent with that of field stars.

We also identified seven Jupiters around stars with $R_\star \lesssim 1.5\,R_\odot$ and estimated a fraction $f_\star = 0.19 \pm 0.07$ per cent for this kind

[8] https://archive.stsci.edu/hlsp/pathos.

of planets, significantly smaller than what estimated for field stars (e.g. Fressin et al. 2013). Two partially compensating effects (completeness of our detection method and false-positive rate) make our results still provisional.

The analysis of the light curves of open cluster members in the northern ecliptic hemisphere, as also the analysis of cluster members that will be observed during the *TESS* extended mission(s), will be important for a better estimate of planet fraction in cluster stars. Spectroscopic follow-up, when feasible, is mandatory as well, in order to confirm the planetary nature and derive the exoplanet masses and search for a correlation between planet composition and cluster properties.

ACKNOWLEDGEMENTS

DN acknowledges support from the French Centre National d'Etudes Spatiales (CNES). DN and GP recognize partial support by UNIPD/DFA Dipartimental project PIOT_SID17_01. GP, VG, LM, MM, and DN acknowledge support from PLATO ASI-INAF agreements nos 2015-019-R0-2015 and 2015-019-R.1-2018. LB, GP, and DN acknowledge the funding support from CHEOPS ASI-INAF agreement no. 2019-29-HH.0. LRB acknowledges support by MIUR under PRIN program #2017Z2HSMF. The authors warmly thank the anonymous referee for the prompt and careful reading of our paper.

REFERENCES

Alard C., Lupton R. H., 1998, ApJ, 503, 325
Anderson J. et al., 2008, AJ, 135, 2055
Bailer-Jones C. A. L., Rybizki J., Fouesneau M., Mantelet G., Andrae R., 2018, AJ, 156, 58
Bailey J. I., Mateo M., White R. J., Shectman S. A., Crane J. D., 2018, MNRAS, 475, 1609
Barros S. C. C., Demangeon O., Deleuil M., 2016, A&A, 594, A100
Bellini A., Anderson J., Bedin L. R., King I. R., van der Marel R. P., Piotto G., Cool A., 2017, ApJ, 842, 6
Benatti S. et al., 2019, A&A, 630, A81
Bica E., Bonatto C., 2011, A&A, 530, A32
Binney J. et al., 2014, MNRAS, 437, 351
Borucki W. J. et al., 2010, Science, 327, 977
Bossini D. et al., 2019, A&A, 623, A108
Bouma L. G., Hartman J. D., Bhatti W., Winn J. N., Bakos G. Á., 2019, ApJS, 245, 13
Brucalassi A. et al., 2014, A&A, 561, L9
Brucalassi A. et al., 2016, A&A, 592, L1
Brucalassi A. et al., 2017, A&A, 603, A85
Cantat-Gaudin T. et al., 2018, A&A, 618, A93
Chang S. W., Byun Y. I., Hartman J. D., 2015, AJ, 149, 135
Ciardi D. R. et al., 2018, AJ, 155, 10
Claret A., 2018, A&A, 618, A20
Cloutier R., 2019, AJ, 158, 81
Curtis J. L. et al., 2018, AJ, 155, 173
David T. J. et al., 2016a, AJ, 151, 112
David T. J. et al., 2016b, Nature, 534, 658
David T. J. et al., 2018, AJ, 156, 302
Foreman-Mackey D., Hogg D. W., Lang D., Goodman J., 2013, PASP, 125, 306
Fressin F. et al., 2013, ApJ, 766, 81
Gaia Collaboration, 2018, A&A, 616, A1
Gaidos E. et al., 2017, MNRAS, 464, 850
Gaidos E. et al., 2020, MNRAS, 495, 650
Gilliland R. L., 2004, ACS Technical Report 2004-01, ACS CCD Gains, Full Well Depths, and Linearity up to and Beyond Saturation
Gilliland R. L., Rajan A., Deustua S., 2010, WFC3 Technical Report 2010-10, WFC3 UVIS Full Well Depths, and Linearity Near and Beyond Saturation
Hidalgo S. L. et al., 2018, ApJ, 856, 125
Hippke M., Heller R., 2019, A&A, 623, A39
Howell S. B. et al., 2014, PASP, 126, 398
Kharchenko N. V., Piskunov A. E., Schilbach E., Röser S., Scholz R. D., 2016, A&A, 585, A101
Kipping D. M., 2010, MNRAS, 408, 1758
Kipping D. M., 2013, MNRAS, 435, 2152
Kreidberg L., 2015, PASP, 127, 1161
Lallement R. et al., 2018, A&A, 616, A132
Libralato M., Bedin L. R., Nardiello D., Piotto G., 2016a, MNRAS, 456, 1137
Libralato M. et al., 2016b, MNRAS, 463, 1780
Malavolta L. et al., 2016, A&A, 588, A118
Malavolta L. et al., 2018, AJ, 155, 107
Mann A. W. et al., 2016a, ApJ, 818, 46
Mann A. W. et al., 2016b, AJ, 152, 61
Mann A. W. et al., 2017, AJ, 153, 64
Mann A. W. et al., 2018, AJ, 155, 4
Meibom S. et al., 2013, Nature, 499, 55
Moré J. J., Garbow B. S., Hillstrom K. E., 1980, ANL Technical Report 80-74, User Guide for MINPACK-1. Argonne National Laboratory, Argonne, IL
Nardiello D. et al., 2015a, MNRAS, 447, 3536
Nardiello D. et al., 2015b, MNRAS, 451, 312
Nardiello D., Libralato M., Bedin L. R., Piotto G., Borsato L., Granata V., Malavolta L., Nascimbeni V., 2016a, MNRAS, 463, 1831
Nardiello D., Libralato M., Bedin L. R., Piotto G., Ochner P., Cunial A., Borsato L., Granata V., 2016b, MNRAS, 455, 2337
Nardiello D. et al., 2018, MNRAS, 481, 3382
Nardiello D. et al., 2019, MNRAS, 490, 3806 (Paper I)
Netopil M., Paunzen E., Heiter U., Soubiran C., 2016, A&A, 585, A150
Newton E. R. et al., 2019, ApJ, 880, L17
Obermeier C. et al., 2016, AJ, 152, 223
Pepper J. et al., 2017, AJ, 153, 177
Pope B. J. S., Parviainen H., Aigrain S., 2016, MNRAS, 461, 3399
Quinn S. N. et al., 2012, ApJ, 756, L33
Quinn S. N. et al., 2014, ApJ, 787, 27
Ricker G. R. et al., 2015, J. Astron. Telesc. Instrum. Syst., 1, 014003
Sato B. et al., 2007, ApJ, 661, 527
Silverman B. W., 1986, Density Estimation for Statistics and Data Analysis, Chapman and Hall, London
Soares-Furtado M., Hartman J. D., Bakos G. Á., Huang C. X., Penev K., Bhatti W., 2017, PASP, 129, 044501
Soares-Furtado M., Hartman J. D., Bhatti W., Bouma L. G., Barna T., Bakos G. Á., 2020, ApJS, 246, 15
Stassun K. G. et al., 2019, AJ, 158, 138
Sullivan P. W. et al., 2015, ApJ, 809, 77
Vanderburg A. et al., 2018, AJ, 156, 46
Wallace J. J., Hartman J. D., Bakos G. Á., Bhatti W., 2019, ApJS, 244, 12

SUPPORTING INFORMATION

Supplementary data are available at https://archive.stsci.edu/hlsp/pathos.

Please note: Oxford University Press is not responsible for the content or functionality of any supporting materials supplied by the authors. Any queries (other than missing material) should be directed to the corresponding author for the article.

APPENDIX A: LIGHT-CURVE MODELLING AND EXOPLANET PARAMETER ESTIMATE

Table A1. Results of transit modelling.

TIC	PATHOS	Cluster	P (d)	T_0 (BTJD)	$R_p/R_\star$	b	$a/R_\star$	$\rho_\star$ ($\rho_\odot$)	LD$_{c1}$	LD$_{c2}$	i (°)	R_p (R_J)	R_p ($R_\oplus$)	Note
0030654608	2	Muzzio 1	$2.4955^{+0.0003}_{-0.0003}$	$1519.662^{+0.009}_{-0.009}$	$0.048^{+0.014}_{-0.009}$	$0.96^{+0.03}_{-0.16}$	$3.7^{+0.6}_{-0.6}$	$0.11^{+0.06}_{-0.04}$	$0.38^{+0.35}_{-0.26}$	$0.18^{+0.32}_{-0.28}$	$71.7^{+5.2}_{-13.6}$	$2.5^{+1.0}_{-0.7}$	$28.6^{+10.8}_{-8.0}$	
0039291805	3	NGC 2112	$7.1719^{+0.0057}_{-0.0059}$	$1469.033^{+0.009}_{-0.009}$	$0.190^{+0.064}_{-0.018}$	$0.69^{+0.21}_{-0.40}$	$14.5^{+0.6}_{-0.6}$	$0.80^{+0.10}_{-0.10}$	$0.31^{+0.05}_{-0.05}$	$0.29^{+0.05}_{-0.05}$	$87.1^{+1.2}_{-0.8}$	$2.1^{+0.7}_{-0.2}$	$23.5^{+7.9}_{-2.6}$	
0042524156	4	ASCC 88	$10.0130^{+0.0025}_{-0.0026}$	$1631.474^{+0.005}_{-0.006}$	$0.125^{+0.024}_{-0.019}$	$0.94^{+0.04}_{-0.06}$	$12.0^{+1.4}_{-1.8}$	$0.23^{+0.09}_{-0.09}$	$0.18^{+0.12}_{-0.11}$	$0.16^{+0.13}_{-0.12}$	$84.0^{+1.6}_{-3.8}$	$3.5^{+0.8}_{-0.7}$	$39.1^{+9.5}_{-7.3}$	
0080317933	5	Collinder 292	$3.2098^{+0.0006}_{-0.0006}$	$1625.529^{+0.003}_{-0.003}$	$0.232^{+0.006}_{-0.005}$	$0.39^{+0.17}_{-0.24}$	$6.3^{+0.5}_{-0.6}$	$0.32^{+0.09}_{-0.09}$	$0.19^{+0.05}_{-0.05}$	$0.23^{+0.05}_{-0.05}$	$86.3^{+2.2}_{-1.8}$	$4.1^{+0.5}_{-0.3}$	$45.8^{+5.4}_{-3.8}$	
0088977253	6	NGC 2548	$2.7677^{+0.0004}_{-0.0004}$	$1492.708^{+0.004}_{-0.004}$	$0.146^{+0.048}_{-0.016}$	$0.85^{+0.11}_{-0.31}$	$6.6^{+0.4}_{-0.5}$	$0.50^{+0.10}_{-0.10}$	$0.27^{+0.05}_{-0.05}$	$0.28^{+0.05}_{-0.05}$	$78.1^{+2.7}_{-4.3}$	$2.1^{+0.6}_{-0.3}$	$23.0^{+7.1}_{-3.2}$	TOI-496
0092835691	7	SAI 91	$22.3661^{+0.0067}_{-0.0069}$	$1527.825^{+0.007}_{-0.007}$	$0.214^{+0.034}_{-0.033}$	$0.92^{+0.05}_{-0.07}$	$20.0^{+2.5}_{-3.1}$	$0.22^{+0.09}_{-0.09}$	$0.19^{+0.05}_{-0.05}$	$0.23^{+0.05}_{-0.05}$	$85.4^{+1.3}_{-2.9}$	$4.4^{+1.0}_{-0.8}$	$49.8^{+11.2}_{-9.3}$	
0094589619	8	NGC 2437	$12.0829^{+0.0045}_{-0.0047}$	$1496.198^{+0.004}_{-0.004}$	$0.187^{+0.062}_{-0.019}$	$0.81^{+0.14}_{-0.39}$	$17.6^{+1.1}_{-1.2}$	$0.50^{+0.10}_{-0.10}$	$0.24^{+0.05}_{-0.05}$	$0.26^{+0.05}_{-0.05}$	$84.9^{+1.3}_{-1.9}$	$2.7^{+0.8}_{-0.4}$	$30.4^{+9.4}_{-4.0}$	
0125414447	9	NGC 2323	$3.7069^{+0.0008}_{-0.0008}$	$1493.200^{+0.004}_{-0.004}$	$0.229^{+0.052}_{-0.035}$	$0.88^{+0.09}_{-0.10}$	$10.4^{+0.3}_{-0.3}$	$1.09^{+0.10}_{-0.10}$	$0.32^{+0.05}_{-0.05}$	$0.30^{+0.05}_{-0.05}$	$85.4^{+0.5}_{-0.8}$	$2.2^{+0.5}_{-0.4}$	$25.1^{+5.7}_{-4.0}$	
0126600730	10	Haffner 14	$6.2991^{+0.0067}_{-0.0067}$	$1497.305^{+0.011}_{-0.009}$	$0.102^{+0.027}_{-0.010}$	$0.75^{+0.18}_{-0.46}$	$9.3^{+1.0}_{-1.2}$	$0.27^{+0.10}_{-0.09}$	$0.15^{+0.05}_{-0.05}$	$0.20^{+0.05}_{-0.05}$	$84.7^{+1.9}_{-2.4}$	$2.1^{+0.7}_{-0.3}$	$23.8^{+8.0}_{-3.7}$	
0144995073	11	NGC 2669	$20.0207^{+0.0051}_{-0.0050}$	$1518.823^{+0.005}_{-0.005}$	$0.240^{+0.066}_{-0.038}$	$0.83^{+0.12}_{-0.34}$	$25.6^{+1.4}_{-1.6}$	$0.56^{+0.10}_{-0.10}$	$0.27^{+0.05}_{-0.05}$	$0.28^{+0.05}_{-0.05}$	$84.9^{+1.4}_{-2.3}$	$3.2^{+0.8}_{-0.5}$	$36.0^{+9.5}_{-6.1}$	
0147069011	12	Alessi 8	$7.3270^{+0.0019}_{-0.0018}$	$1628.559^{+0.004}_{-0.004}$	$0.448^{+0.035}_{-0.045}$	$0.38^{+0.22}_{-0.25}$	$13.9^{+0.6}_{-0.7}$	$0.67^{+0.10}_{-0.10}$	$0.28^{+0.05}_{-0.05}$	$0.29^{+0.05}_{-0.05}$	$86.8^{+1.9}_{-1.6}$	$5.4^{+0.5}_{-0.6}$	$61.0^{+5.6}_{-6.5}$	
0147426828	13	NGC 2318	$1.4618^{+0.0002}_{-0.0002}$	$1492.845^{+0.004}_{-0.004}$	$0.221^{+0.047}_{-0.037}$	$0.89^{+0.08}_{-0.12}$	$4.2^{+0.3}_{-0.3}$	$0.47^{+0.09}_{-0.09}$	$0.25^{+0.05}_{-0.05}$	$0.27^{+0.05}_{-0.05}$	$76.2^{+2.2}_{-3.9}$	$3.2^{+0.7}_{-0.6}$	$35.9^{+7.6}_{-6.4}$	
0153734545	14	NGC 2527	$3.2196^{+0.0003}_{-0.0003}$	$1493.665^{+0.008}_{-0.008}$	$0.187^{+0.034}_{-0.025}$	$0.92^{+0.06}_{-0.06}$	$4.5^{+0.8}_{-0.6}$	$0.11^{+0.07}_{-0.04}$	$0.22^{+0.05}_{-0.05}$	$0.25^{+0.05}_{-0.05}$	$78.1^{+3.1}_{-5.1}$	$4.8^{+1.2}_{-0.9}$	$53.7^{+13.7}_{-10.4}$	
0153735144	15	NGC 2527	$3.7785^{+0.0003}_{-0.0003}$	$1493.406^{+0.002}_{-0.002}$	$0.178^{+0.006}_{-0.004}$	$0.37^{+0.24}_{-0.25}$	$7.8^{+0.5}_{-0.6}$	$0.44^{+0.10}_{-0.10}$	$0.26^{+0.05}_{-0.05}$	$0.27^{+0.05}_{-0.05}$	$84.4^{+3.5}_{-2.6}$	$2.6^{+0.2}_{-0.2}$	$29.0^{+2.7}_{-2.1}$	
0159059181	16	NGC 2112	$5.2167^{+0.0020}_{-0.0020}$	$1471.198^{+0.005}_{-0.005}$	$0.162^{+0.048}_{-0.025}$	$0.87^{+0.09}_{-0.31}$	$9.3^{+0.7}_{-0.8}$	$0.40^{+0.10}_{-0.09}$	$0.28^{+0.05}_{-0.05}$	$0.28^{+0.05}_{-0.05}$	$82.5^{+1.8}_{-3.3}$	$2.4^{+0.7}_{-0.4}$	$27.0^{+7.6}_{-4.8}$	
0181602717	17	NGC 2671	$2.4557^{+0.0002}_{-0.0002}$	$1517.489^{+0.009}_{-0.009}$	$0.246^{+0.030}_{-0.034}$	$0.93^{+0.05}_{-0.06}$	$5.9^{+0.4}_{-0.5}$	$0.46^{+0.10}_{-0.10}$	$0.25^{+0.05}_{-0.05}$	$0.25^{+0.05}_{-0.05}$	$83.2^{+0.9}_{-1.5}$	$3.6^{+0.5}_{-0.5}$	$40.2^{+6.0}_{-5.8}$	
0236084210	18	ASCC 85	$5.3465^{+0.0016}_{-0.0016}$	$1631.974^{+0.004}_{-0.004}$	$0.182^{+0.035}_{-0.028}$	$0.91^{+0.06}_{-0.07}$	$9.8^{+0.6}_{-0.8}$	$0.44^{+0.09}_{-0.09}$	$0.15^{+0.05}_{-0.05}$	$0.18^{+0.05}_{-0.05}$	$83.9^{+0.9}_{-1.8}$	$3.3^{+0.6}_{-0.5}$	$36.6^{+7.2}_{-5.8}$	
0300362600	19	NGC 5316	$11.6556^{+0.0073}_{-0.0075}$	$1602.169^{+0.003}_{-0.004}$	$0.213^{+0.005}_{-0.005}$	$0.20^{+0.18}_{-0.14}$	$13.7^{+1.5}_{-1.4}$	$0.25^{+0.09}_{-0.07}$	$0.15^{+0.05}_{-0.05}$	$0.19^{+0.05}_{-0.05}$	$89.2^{+0.6}_{-0.8}$	$4.6^{+0.5}_{-0.5}$	$51.3^{+6.0}_{-5.2}$	
0306385801	20	NGC 3532	$14.0367^{+0.0020}_{-0.0018}$	$1575.028^{+0.003}_{-0.003}$	$0.110^{+0.003}_{-0.002}$	$0.48^{+0.19}_{-0.30}$	$15.2^{+1.8}_{-2.3}$	$0.24^{+0.10}_{-0.09}$	$0.17^{+0.05}_{-0.05}$	$0.21^{+0.05}_{-0.05}$	$86.9^{+1.6}_{-2.0}$	$2.3^{+0.4}_{-0.3}$	$25.5^{+4.5}_{-2.8}$	
0308538095	21	NGC 2516	$11.6929^{+0.0002}_{-0.0002}$	$1420.294^{+0.002}_{-0.002}$	$0.130^{+0.004}_{-0.003}$	$0.40^{+0.24}_{-0.27}$	$18.6^{+0.9}_{-1.0}$	$0.63^{+0.10}_{-0.10}$	$0.28^{+0.05}_{-0.05}$	$0.29^{+0.05}_{-0.05}$	$84.6^{+3.2}_{-2.0}$	$1.6^{+0.1}_{-0.1}$	$18.2^{+1.2}_{-1.0}$	
0317536999	22	Ruprecht 94	$5.8557^{+0.0007}_{-0.0007}$	$1576.007^{+0.004}_{-0.004}$	$0.178^{+0.037}_{-0.025}$	$0.90^{+0.06}_{-0.08}$	$10.4^{+0.7}_{-0.8}$	$0.44^{+0.09}_{-0.09}$	$0.15^{+0.05}_{-0.05}$	$0.17^{+0.05}_{-0.05}$	$84.5^{+0.8}_{-1.5}$	$3.2^{+0.7}_{-0.5}$	$36.1^{+7.9}_{-5.7}$	
0372913337	23	NGC 2516	$1.7860^{+0.0001}_{-0.0001}$	$1325.341^{+0.006}_{-0.006}$	$0.045^{+0.011}_{-0.004}$	$0.96^{+0.03}_{-0.10}$	$3.7^{+0.5}_{-0.5}$	$0.22^{+0.09}_{-0.07}$	$0.15^{+0.05}_{-0.05}$	$0.19^{+0.05}_{-0.05}$	$71.1^{+4.9}_{-16.1}$	$1.1^{+0.3}_{-0.2}$	$11.8^{+3.5}_{-2.4}$	
0389927567	24	Melotte 101	$6.9408^{+0.0009}_{-0.0010}$	$1575.805^{+0.006}_{-0.006}$	$0.261^{+0.058}_{-0.036}$	$0.85^{+0.10}_{-0.14}$	$10.0^{+1.1}_{-1.3}$	$0.28^{+0.10}_{-0.09}$	$0.15^{+0.05}_{-0.05}$	$0.17^{+0.05}_{-0.05}$	$80.1^{+2.7}_{-5.0}$	$5.7^{+1.3}_{-1.0}$	$64.1^{+14.6}_{-11.0}$	
0410450228	25	NGC 2516	$15.7784^{+0.0004}_{-0.0004}$	$1420.250^{+0.004}_{-0.004}$	$0.095^{+0.022}_{-0.010}$	$0.93^{+0.04}_{-0.04}$	$21.0^{+1.2}_{-1.5}$	$0.50^{+0.09}_{-0.10}$	$0.22^{+0.05}_{-0.05}$	$0.25^{+0.05}_{-0.05}$	$87.1^{+0.4}_{-0.9}$	$1.4^{+0.3}_{-0.2}$	$15.7^{+3.7}_{-2.0}$	TOI-681
0413809436	26	NGC 5925	$2.7030^{+0.0006}_{-0.0006}$	$1627.336^{+0.003}_{-0.003}$	$0.233^{+0.011}_{-0.007}$	$0.52^{+0.18}_{-0.31}$	$6.4^{+0.4}_{-0.5}$	$0.49^{+0.10}_{-0.10}$	$0.18^{+0.05}_{-0.05}$	$0.23^{+0.05}_{-0.05}$	$84.3^{+2.8}_{-1.9}$	$3.6^{+0.4}_{-0.3}$	$40.2^{+4.4}_{-2.9}$	
0419091401	27	Ruprecht 48	$12.7071^{+0.0024}_{-0.0023}$	$1499.685^{+0.007}_{-0.007}$	$0.188^{+0.047}_{-0.011}$	$0.75^{+0.16}_{-0.28}$	$11.9^{+2.0}_{-2.2}$	$0.14^{+0.08}_{-0.06}$	$0.16^{+0.10}_{-0.09}$	$0.21^{+0.10}_{-0.10}$	$81.4^{+3.3}_{-7.6}$	$5.2^{+1.5}_{-0.9}$	$57.9^{+17.2}_{-10.6}$	
0432564189	28	Ruprecht 82	$3.7611^{+0.0003}_{-0.0003}$	$1546.783^{+0.004}_{-0.004}$	$0.120^{+0.008}_{-0.005}$	$0.64^{+0.20}_{-0.42}$	$6.5^{+0.7}_{-0.8}$	$0.27^{+0.09}_{-0.09}$	$0.16^{+0.05}_{-0.05}$	$0.21^{+0.05}_{-0.05}$	$76.1^{+5.6}_{-9.3}$	$2.4^{+0.4}_{-0.3}$	$27.3^{+5.0}_{-3.1}$	
0450610413	29	Harvard 5	$10.6780^{+0.0027}_{-0.0027}$	$1600.682^{+0.004}_{-0.004}$	$0.176^{+0.004}_{-0.004}$	$0.21^{+0.19}_{-0.15}$	$15.3^{+1.2}_{-1.2}$	$0.42^{+0.10}_{-0.09}$	$0.15^{+0.05}_{-0.05}$	$0.20^{+0.05}_{-0.05}$	$89.2^{+0.6}_{-0.7}$	$3.0^{+0.3}_{-0.2}$	$33.9^{+2.9}_{-2.5}$	
0460205581	30	IC 2602	$8.3252^{+0.0006}_{-0.0006}$	$1574.271^{+0.002}_{-0.002}$	$0.059^{+0.005}_{-0.002}$	$0.57^{+0.26}_{-0.35}$	$16.9^{+0.6}_{-0.6}$	$0.94^{+0.10}_{-0.10}$	$0.31^{+0.05}_{-0.05}$	$0.30^{+0.05}_{-0.05}$	$83.4^{+2.7}_{-2.4}$	$0.6^{+0.1}_{-0.1}$	$6.9^{+0.6}_{-0.4}$	TOI-837
0460950389	31	IC 2602	$2.8622^{+0.0004}_{-0.0004}$	$1572.224^{+0.004}_{-0.004}$	$0.042^{+0.002}_{-0.002}$	$0.30^{+0.26}_{-0.20}$	$9.4^{+0.2}_{-0.2}$	$1.37^{+0.10}_{-0.10}$	$0.43^{+0.05}_{-0.05}$	$0.38^{+0.05}_{-0.05}$	$88.1^{+1.3}_{-1.3}$	$0.3^{+0.1}_{-0.1}$	$3.8^{+0.2}_{-0.2}$	
0462004618	32	NGC 3114	$2.3669^{+0.0001}_{-0.0001}$	$1544.599^{+0.004}_{-0.004}$	$0.172^{+0.027}_{-0.024}$	$0.93^{+0.04}_{-0.05}$	$5.1^{+0.4}_{-0.5}$	$0.32^{+0.08}_{-0.09}$	$0.15^{+0.05}_{-0.05}$	$0.20^{+0.05}_{-0.05}$	$78.2^{+1.9}_{-3.9}$	$3.3^{+0.6}_{-0.5}$	$37.3^{+6.6}_{-5.9}$	
0748919024	33	Ruprecht 151	$2.5395^{+0.0007}_{-0.0006}$	$1494.064^{+0.004}_{-0.004}$	$0.118^{+0.004}_{-0.003}$	$0.37^{+0.26}_{-0.25}$	$6.0^{+0.4}_{-0.5}$	$0.46^{+0.10}_{-0.11}$	$0.25^{+0.05}_{-0.05}$	$0.27^{+0.05}_{-0.05}$	$86.9^{+2.1}_{-1.7}$	$1.7^{+0.2}_{-0.1}$	$19.2^{+1.9}_{-1.4}$	
1036769612	34	Trumpler 22	$7.4732^{+0.0014}_{-0.0013}$	$1599.298^{+0.005}_{-0.005}$	$0.111^{+0.005}_{-0.004}$	$0.37^{+0.24}_{-0.25}$	$13.4^{+1.3}_{-1.6}$	$0.57^{+0.19}_{-0.19}$	$0.24^{+0.05}_{-0.05}$	$0.27^{+0.05}_{-0.05}$	$88.1^{+1.2}_{-1.2}$	$1.5^{+0.2}_{-0.2}$	$17.0^{+2.6}_{-1.7}$	

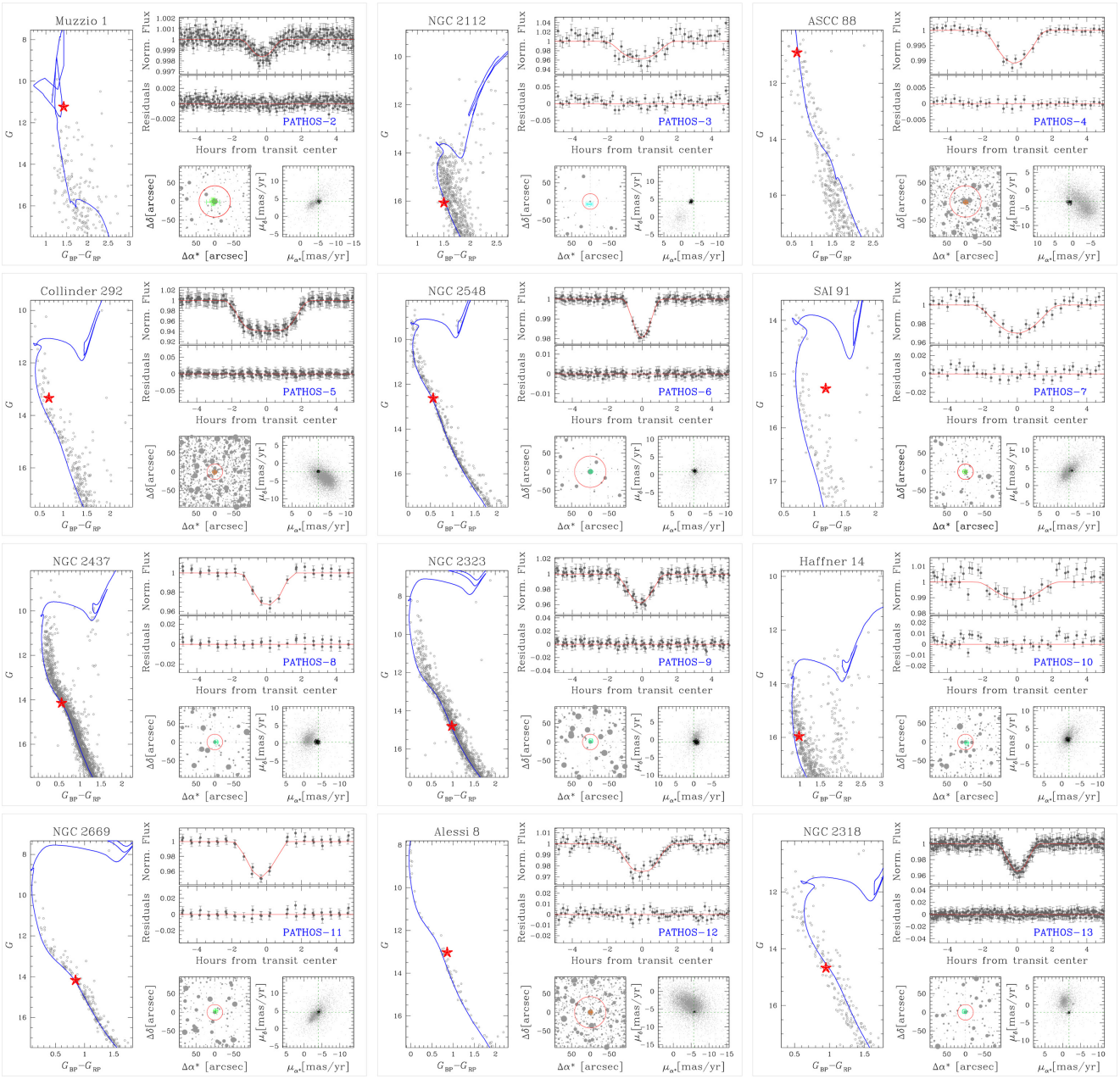

Figure A1. Overview on the candidate exoplanets PATHOS-2–PATHOS-13. On the left-hand panel, the G versus $G_{BP} - G_{RP}$ CMD of the cluster that hosts the target star (red star) and the isochrone (blue) fitted with the cluster parameters listed in Table 1. The top right-hand panel shows the folded light curve (grey points) of the candidate and the model (in red) found with PYORBIT; the middle panel shows the difference between the observed points and the model. The bottom left-hand panel shows the 95 × 95 arcsec^2 finding chart centred on the target star; the red circle shows the aperture adopted to extract photometry, and crosses show the in/out-of transit difference centroid, colour-coded as in Fig. 6. The bottom right-hand panel is the vector-point diagram, centred on the target star, for all the stars that are within 10 arcmin from the target star; black points show the cluster members listed in the catalogue by Cantat-Gaudin et al. (2018).

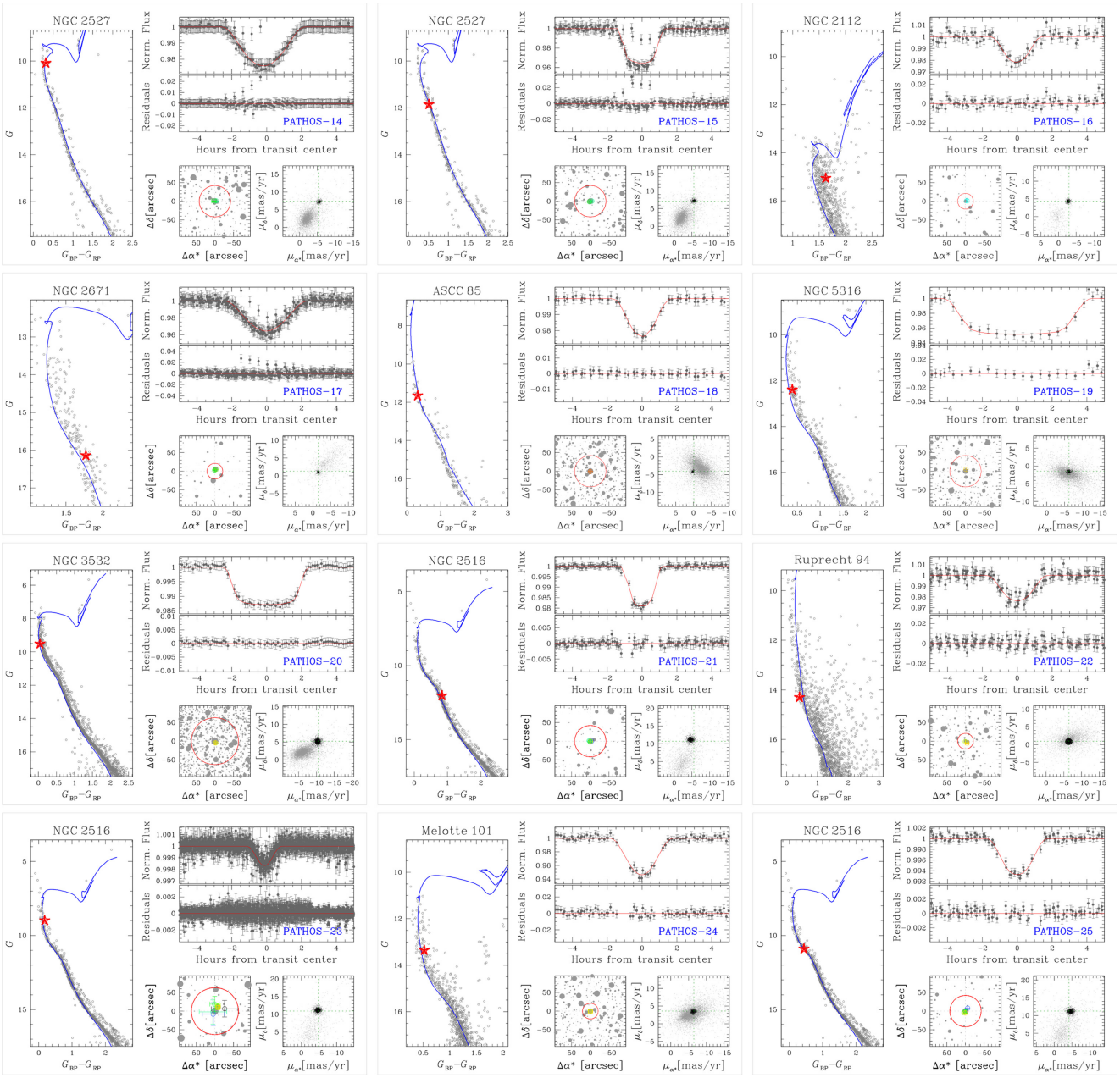

Figure A2. As in Fig. A1, but for PATHOS-14 – PATHOS-25.

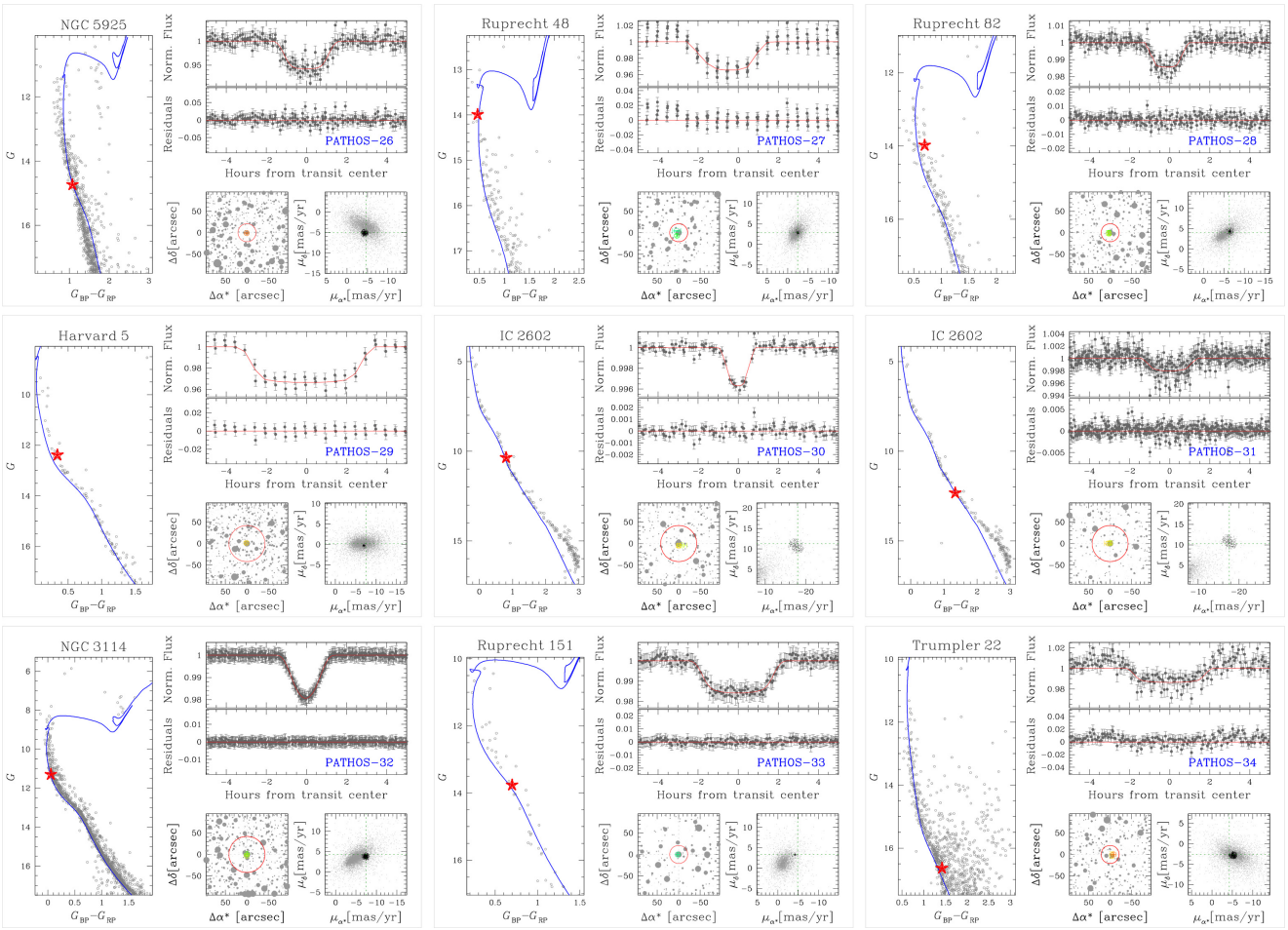

Figure A3. As in Fig. A1, but for PATHOS-26–PATHOS-34.

This paper has been typeset from a TEX/LATEX file prepared by the author.